In situ architecture of Opa1-dependent mitochondrial cristae remodeling

Authors

Michelle Y. Fry[1,2,†], Paula P. Navarro[1,2,†], Pusparanee Hakim[1], Virly Y. Ananda[1], Xingping Qin[3,10,11], Juan C. Landoni[4], Sneha Rath[1], Zintis Inde[3,10,11], Camila Makhlouta Lugo[1], Bridget E. Luce[1], Yifan Ge[1,2,5], Julie L. McDonald[1,6], Ilzat Ali[1,2], Leillani L. Ha[7,8], Benjamin P. Kleinstiver[7,8,9], David C. Chan[10], Kristopher A. Sarosiek[3,11,12], and Luke H. Chao[1,2*]

Affiliations

[1] Department of Molecular Biology, Massachusetts General Hospital, Boston, USA

[2] Department of Genetics, Blavatnik Institute, Harvard Medical School, Boston, USA

[3] John B. Little Center for Radiation Sciences, Harvard T.H. Chan School of Public Health, Boston, USA

[4] Institute of Physics, École Polytechnique Fédérale de Lausanne (EPFL), Lausanne, Switzerland

[5] Current address: Interdisciplinary Research Center of Biology and Chemistry, Shanghai Institute of Organic Chemistry, Chinese Academy of Science, China.

[6] Current address: Massachusetts Institute of Technology, Biology, Cambridge, USA

[7] Center for Genomic Medicine, Massachusetts General Hospital, Boston, USA

[8] Department of Pathology, Massachusetts General Hospital, Boston, USA

[9] Department of Pathology, Harvard Medical School, Boston, USA

[10] Division of Biology and Biological Engineering, California Institute of Technology, Pasadena, USA

[11] Molecular and Integrative Physiological Sciences (MIPS) Program, Harvard T.H. Chan School of Public Health, Boston, USA

[12] Lab of Systems Pharmacology, Harvard Program in Therapeutic Science, Department of Systems Biology, Harvard Medical School, Boston, MA, USA

[†] These authors contributed equally, sequence was determined alphabetically. Co-first authors have agreed each reserves the right to adjust order in their CVs and public presentations of the work.

* To whom correspondence should be addressed

Luke H. Chao

Department of Molecular Biology, Massachusetts General Hospital, Boston, USA

Department of Genetics, Harvard Medical School, Boston, USA

e-mail: chao@molbio.mgh.harvard.edu

Keywords

Cristae remodeling, Mitochondrial biology, Cryo-electron tomography, Cryo-focused ion beam milling

Abstract

Cristae membrane state plays a central role in regulating mitochondrial function and cellular metabolism. The protein Optic atrophy 1 (Opa1) is an important crista remodeler that exists as two forms in the mitochondrion, a membrane-anchored long form (l-Opa1) and a processed short form (s-Opa1). The mechanisms for how Opa1 influences cristae shape have remained unclear due to lack of native three-dimensional views of cristae. We perform *in situ* cryo-electron tomography of cryo-focused ion beam milled mouse embryonic fibroblasts with defined Opa1 states to understand how each form of Opa1 influences cristae architecture. In our tomograms, we observe a variety of cristae shapes with distinct trends dependent on s-Opa1:l-Opa1 balance. Increased l-Opa1 levels promote cristae stacking and elongated mitochondria while increased s-Opa1 levels correlated with irregular cristae packing and round mitochondria shape. Functional assays indicate a role for l-Opa1 in wild-type apoptotic and calcium handling responses, and compromised respiratory function under Opa1 imbalance. In summary, we provide three-dimensional visualization of cristae architecture to reveal relationships between mitochondrial ultrastructure and cellular function dependent on Opa1-mediated membrane remodeling.

Highlights

- *In situ* ultrastructural characterization of mitochondrial cristae with different forms of Opa1.
- Mitochondria with predominantly l-Opa1 show crista stacking, longer cristae, reduced globular cristae and an absence of tubular cristae.
- Mitochondria with mostly s-Opa1 showed irregular cristae packing with wider cristae junctions and narrower cristae.
- l-Opa1 expressing cells with WT-like cristae junction properties, show wild-type apoptotic response and calcium handling.
- Imbalance in Opa1 processing show compromised respiratory function and an increase in amorphous cristae.

Introduction

Mitochondria play essential roles in energy production, metabolism and signaling, which drive diverse biological functions and processes of the cell (Chandel, 2014; Spinelli & Haigis, 2018; Picard & Shirihai, 2022). The organelle undergoes membrane remodeling during homeostatic steady-state conditions through fusion and fission to generate a dynamic and responsive reticulum (Twig *et al*, 2008; Mishra *et al*, 2014; Mishra & Chan, 2016). Mitochondrial ultrastructure is defined by a double-membrane architecture with an outer (OMM) and inner mitochondrial membrane (IMM). The IMM can be divided into three sub-regions, the cristae folds, the inner boundary membrane (IBM) and the cristae junctions (CJ), which separates cristae from the IBM. Cristae are enriched with electron transport chain (ETC) proteins, making them a hub for energy production (Schägger & Pfeiffer, 2000). In metazoans, cristae are mostly lamellar or tubular (Hashimi, 2019) and undergo dramatic rearrangements in response to stress and during initiation of apoptotic cell death (Frey & Mannella, 2000; Mannella, 2006; Zick *et al*, 2009). Despite longstanding interest in mitochondrial morphogenesis and major advances in understanding of mitochondrial structure and function (Friedman & Nunnari, 2014), regulation of cristae remodeling remains poorly understood.

Relevant proteins for cristae remodeling include ATP synthase (Blum *et al*, 2019), optic atrophy protein 1 (Opa1) and the mitochondrial contact site and cristae organizing system (MICOS) (Friedman & Nunnari, 2014; Laan *et al*, 2016). Opa1 is responsible for fusing the IMM during mitochondrial fusion and is also implicated in cristae remodeling. Inner-membrane proteases, such as Oma1, Yme1L, and ParI, process Opa1 to generate a ‘soluble’ form that lacks the N-terminal transmembrane (TM) segment (s-Opa1) (Song *et al*, 2007; Anand *et al*, 2014). This processing results in two forms of Opa1 in the mitochondria: the soluble short form (s-Opa1) and the unprocessed, full N-terminal TM anchored long form (l-Opa1). We previously showed that stoichiometric levels of both l- and s-Opa1 are required for fast and efficient membrane fusion *in vitro* (Ge *et al*, 2020); however, *in situ* ultrastructural understanding of how cristae shape is maintained by each Opa1 form is lacking.

Previous work used transmission electron microscopy (TEM) imaging of chemically fixed and heavy metal-stained cells to investigate the role of Opa1 in cristae shape. Knocking-down Opa1 induced more disorganized, globular and hyper-convex cristae, whereas over expression of Opa1 resulted in narrower cristae and CJs (Frezza *et al*, 2006). Initial steps of apoptosis involve release of cytochrome c from the cristae lumen, where ~85% of the cellular cytochrome c is stored (Scorrano *et al*, 2002). Expression of wild-type (WT) Opa1 was reported to protect against apoptosis by restricting cytochrome c release, whereas the loss of Opa1 was reported to result in mitochondria fragmentation and enhanced cytochrome c release (Scorrano *et al*, 2002). Addition of pro-apoptotic peptides resulted in wider CJs

observed in TEM images. These observations suggest the organelle's inner-membrane functional state may be sensitive to the levels of Opa1 present, and the membrane architectures supported by Opa1.

To understand the role of s- and l-Opa1 in cristae architecture and remodeling, we investigated the *in situ* state of mitochondrial membranes in mouse embryonic fibroblasts (MEF) with different levels of s- and l-Opa1, by applying cryo-electron tomography (cryo-ET) on cryo-focused ion beam (cryo-FIB) milled MEF. We used defined cell lines that predominantly contained either l- or s-Opa1 to characterize how mitochondrial membrane organization and shape depend on the expression levels and form of Opa1. Here, we present an extensive characterization of the 3D morphological properties of mitochondrial cristae membranes. We observed that l-Opa1 contributes to crista stacking, longer cristae, a reduction of globular cristae, an absence of tubular cristae and the maintenance of cristae junction widths. We found that the presence of s-Opa1 correlates with tubular cristae, wider cristae junctions, narrower cristae, and irregular cristae packing. Using BH3 profiling, we observed WT-like apoptotic responses only in the cells with l-Opa1. We also found WT-like calcium handling responses in cells expressing mainly l-Opa1 and that both forms of Opa1 are important for normal respiratory function. Our work reveals roles for s- and l-Opa1 beyond mitochondrial fusion and demonstrates that both forms of Opa1 play distinct roles in cristae shape maintenance important for mitochondrial function.

Results

In situ morphology of mitochondria with different Opa1 processing.

We generated cryo-electron tomograms of mitochondria from cryo-FIB milled MEF cell lines that differed in the expression levels and processed states of Opa1, to investigate mitochondrial cristae ultrastructure (**Fig. S1**). In this study, we used five MEF cell lines: (i) wild-type (WT) cells, (ii) cells stably overexpressing Opa1 (Opa1-OE), (iii) a Δ*exon5b* CRISPR MEF line with an Oma1$^{-/-}$ background, which restricts Opa1 cleavage and results in the presence of mostly l-Opa1 (referred to as l-Opa1* in this work), (iv) an Opa1 knock-out (Opa1-KO) line stably expressing the Opa1 isoform 5, which is robustly processed and results in the presence of s-Opa1 (referred to as s-Opa1*) and (v) Opa1-KO cells (Mishra *et al*, 2014; Wang *et al*, 2021) (**Fig. S1)**. While previous studies have characterized mitochondrial ultrastructure, these samples were subjected to chemical fixation and heavy metal staining, which are recognized to perturb cellular membrane state and limit resolution (Bäuerlein & Baumeister, 2021). Thus, we vitrified MEF cell lines to characterize mitochondrial membrane architecture under native conditions. To prepare samples for cryo-ET imaging, we generated ~200-350 nm thick lamellae by cryo-FIB milling (Rigort *et al*, 2012; Mahamid *et al*, 2016), following a previously established imaging pipeline (Navarro *et al*, 2022). A total of 100 tilt-series (WT = 33, Opa1-OE = 7, l-Opa1* = 21, s-Opa1* = 28 and Opa1-KO = 11) were

acquired, aligned and three-dimensionally (3D) reconstructed into tomograms (**Table S1**). Cryo-electron tomograms were denoised using Topaz-Denoise to improve mitochondrial membrane visualization (Bepler *et al*, 2020). It is important to note that cryo-electron tomograms generated by cryo-FIB milling cover a section of the mitochondria contained within the thickness of the lamella, thus, all mitochondria were partially imaged in the Z-axis. In some cases, mitochondria are only partially visible in the XY plane due to the trade-off between resolution and field of view (Navarro, 2022) (**Fig. S2a**). Densities corresponding to the IMM and OMM were 3D segmented in yellow and green, respectively (**Fig.1a, Movies 1-5**).

The generated tomograms provide rich 3D information on mitochondrial morphology. By visual morphological analysis, we classified mitochondria into ellipsoidal, round, partial (when partially imaged in the XY plane) or polygon shape categories. The majority of mitochondria in all cell lines are ellipsoidal, except for s-Opa1* cells, where round mitochondria dominate (**Fig. 1b**), correlating with a smaller apparent mitochondrial area (**Fig. 1c**). Mitochondria in WT cells are larger in area (0.34 ± 0.03 μm^2) than in other cell lines; with smaller mitochondria in l-Opa1* cells (0.2 ± 0.02 μm^2) and significantly smaller mitochondria in Opa1-OE (0.14 ± 0.02 μm^2) and s-Opa1* cells (0.18 ± 0.02 μm^2) (**Fig. 1c**). We measured the mitochondrial volume and the volumes of each subcompartment: the matrix, inner membrane space (IMS) and cristae lumen (CL) (**Fig. S3)**. Our analysis shows that imbalance of l- and s-Opa1 levels results in larger CL volume (**Fig. S3c-f**).

At first glance, we observed differences in matrix contrast between mitochondria from different cell lines in our cryo-ET data. To investigate this further, we quantified the grey scale levels in normalized summed projected images from cryo-electron tomograms (**Fig. S3g)**. We observed denser mitochondrial matrices in Opa1-OE, l-Opa1*, and Opa1-KO mitochondria. For the Opa1-OE mitochondria, the darker measured grey scale value can be attributed to the presence of electron dense deposits within the mitochondrial matrix, likely to be calcium phosphate deposits (Wolf *et al*, 2017; Strubbe-Rivera *et al*, 2021) (**Fig. 1a and S2a white arrowheads, Fig. S3h)**.

We analyzed mitochondrial cristae density (number of cristae/μm^2) in the cryo-electron tomograms. No significant difference was observed in the cristae density between mitochondria in WT and Opa1-KO cells (**Fig. S4a**). All other conditions (Opa1-OE, l-Opa1* and s-Opa1*) resulted in a significant increase in cristae density compared to WT. Such variation was not reflected in the total number of cristae per mitochondria (**Fig. S4b**). This can be explained by the reduction in average mitochondria size (**Fig. 1c**). These observations indicate that altered Opa1 levels or processing can impact the steady-state cristae number in a given mitochondrial volume.

We next characterized how Opa1 processing influences cristae organization. In l-Opa1* cells, we observed organized and parallel oriented cristae, whereas cristae from s-Opa1* cells do not exhibit such

a pattern or organization and frequently cross over one another along the z-axis (**Fig. 1a, S2a and S4c**). Additionally, we observed a subpopulation of mitochondria displaying a stacking cristae phenotype, which we defined as three or more lamellar cristae running in parallel to one another into the mitochondrial matrix throughout the tomogram **(Fig. S4c).** This phenotype was observed at similar levels in WT (23.53%) and s-Opa1* cells (27.27%), but slightly more frequently in Opa1-KO (33.33%) cells. Opa1 overexpression or inhibition of Opa1 processing (l-Opa1*) resulted in a dramatic increase (>50%) of mitochondria with stacking cristae (**Fig. S4d**). These results suggest that homeostatic levels of Opa1 processing maintain WT levels of cristae stacking.

We also used live-cell fluorescence microscopy (FM) and immunofluorescence to assess whole cell mitochondrial network morphology. Consistent with previous FM reports, we observed an almost equal mixture of short and long tubular mitochondrial networks in WT cells and a dramatically fragmented network in Opa1-KO cells (Song *et al*, 2007; Patten *et al*, 2014; Bocca *et al*, 2018) **(Figure S5)**. While fragmented mitochondrial networks were observed in s-Opa1* cells, more elongated tubular networks were observed in l-Opa1* cells correlating with the increased number of round and polygon mitochondria respectively found by cryo-ET (**Fig. 1a-b**). Opa1-OE cells showed longer tubular networks, compared to WT **(Figure S5b)**. These data suggest healthy fusion activity in WT and l-Opa1* cells and corroborate our cryo-ET observations (**Fig. S5, Movie 6**).

In situ cristae ultrastructure

To address questions related to the specific roles for Opa1 forms in cristae morphology, we sought to characterize the dependence of cristae architecture on the form of Opa1 present. Based on their direction relative to the OMM, we quantified cristae as straight or tilted. For some cristae, no connection to the IMM was captured in the tomogram and thus classified as no attachment observed (NAO) (**Fig. 2a**). This is a consequence of all mitochondria being partially imaged in the z-axis, as mentioned above. In Opa1-KO cells fewer cristae were straight compared to WT (**Fig. 2a**). The presence of either form of Opa1 restores the proportion of straight cristae to WT-like levels, while overexpression of Opa1 results in more straight cristae than WT.

Cristae were then classified based on 3D-shape into canonical lamellar, globular, and tubular categories (Harner *et al*, 2016). Across all cell lines, lamellar cristae dominate (**Fig. 2b**). Interestingly, the proportion of lamellar cristae increases in l-Opa1* (81%) and s-Opa1* (77%) cells. Tubular cristae are not observed in l-Opa1* and Opa1-KO cells and are reduced in Opa1-OE (3.24%) and s-Opa1* (2.3%) cells compared to WT (9.6%). Globular cristae are present in all cell lines albeit to a lesser extent when Opa1 expression levels are altered but increased in the absence of Opa1 **(Fig. 2b)**. The proportion of

unusually shaped cristae is similar among WT (27%) and Opa1-OE (30.52%), but reduced in l-Opa1* (17%), s-Opa1* (16.9%) and Opa1-KO (18.9%) cell lines (**Fig. 2b, S2a**).

Unusual cristae were further subclassified into eight defined categories: (i) loop, where cristae curve and connect to IBM via two CJs; (ii) split, where cristae branch into two or more cristae; (iii) straight-across, when cristae are perpendicular and connect to the IBM via two CJs; (iv) amorphous, when cristae display a nebulous morphology; (v) ring, where cristae are circular; (vi) pinched, where cristae show areas where membranes touch; (vii) zipped, when cristae have regions where both membranes merge until both cannot be distinguished; and (viii) vesicular, where material is observed within the cristae (**Fig. S6**). Of these categories only five were observed in WT mitochondria – ring, loop, straight-across, amorphous, and split. The loop phenotype is dominant in WT unusual cristae, but also present in all cell lines (**Fig. S6a**). Pinched and zipped cristae are absent in WT cells but predominant in Opa1-OE cells. Zipped cristae were observed in l-Opa1* cells and only once in s-Opa1* cells, suggesting l-Opa1 may play a role in bridging the two membranes of the cristae for long stretches. In the absence of Opa1, no split or straight across cristae were observed; instead, more cristae fall into the amorphous and vesicular categories. An increase in amorphous cristae were also observed in l-Opa1* and s-Opa1* cells. All cristae shapes were observed in s-Opa1* cells, with roughly a quarter of the unusual cristae falling into the pinched category. Compared to WT, a similar proportion of unusual cristae in s-Opa1* mitochondria fall into the split category. Ring shaped cristae are rare and were not observed in l-Opa1* cells.

To determine the dependence of cristae length and width on the form of Opa1 present, we measured in 3D the length and width of fifty cristae per cell line (**Fig. S7a**). Knocking-out Opa1 results in significantly longer cristae (**Fig. 2c**). This increase in cristae length was not observed in Opa1-OE cells, but was observed in both s-Opa1* and l-Opa1* cells. In s-Opa1* mitochondria, there is a broad distribution of cristae lengths, with a considerable number of longer cristae than WT, which was also observed in Opa1-KO mitochondria. Overexpression of Opa1 does not affect cristae width, but the absence of Opa1 correlates with wider cristae, consistent with a larger proportion of observed globular cristae (**Fig. 2d**). Cristae widths are restored to WT values in l-Opa1* mitochondria, but in s-Opa1* mitochondria cristae are significantly narrower. Though Opa1-OE and l-Opa1* mitochondria have similar average cristae widths to WT mitochondria, a larger variation in cristae widths was observed, with many values falling into 0-5 nm and 9-14 nm ranges (**Fig. 2f**). This suggests that a significant proportion of cristae in Opa1-OE and l-Opa1* mitochondria vary in width, correlating with an increase in the number of zipped or pinched cristae in these cell lines (**Fig. 2e**). Even though cristae width histograms from s-Opa1* and WT mitochondria exhibit a single narrow peak, s-Opa1* mitochondria have tighter cristae (6-15 nm and 9-16 nm, respectively) (**Fig. 2e-f**). In Opa1-KO mitochondria, the cristae width distribution peak ranges from 10-17 nm, with an outlier representing a population of extremely wide cristae also seen in l-Opa1*

mitochondria, particularly a subclass of globular cristae (**Fig. 2b, d-f**). These observations suggest the uniformity of cristae widths observed in WT mitochondria is disrupted by changes in Opa1 expression levels and suppression of Opa1 processing.

Cristae junction morphology by cryo-ET

To gain insight into the role of each Opa1 form at the cristae junction (CJ), we measured and analyzed CJs from summed projected central slices of tomograms for all cell lines. CJs were defined as the site where the crista membrane joins the boundary region of the IMM (**Fig. S7c)**. Compared to WT mitochondria, we observed wider CJs in Opa1-KO mitochondria, consistent with previous TEM data (Scorrano *et al*, 2002) and unaltered CJ widths in Opa1-OE mitochondria (**Fig. 3a**). Intriguingly, we found that CJs are also significantly wider in s-Opa1* mitochondria compared to WT mitochondria (**Fig. 3a**). We did not, however, find any significant difference in CJ widths in l-Opa1* mitochondria. These measurements indicate under steady-state conditions complete processing of Opa1 results in larger CJ widths.

In our initial inspection of our tomograms, we noticed that a greater proportion of cristae in s-Opa1* mitochondria are tilted, i.e. where the crista length is not perpendicular to the IBM (**Fig. 2a**). To further investigate if this tilt occurs at the beginning of the crista or along the length of the cristae, we quantified the angle at the CJ (**Fig. S7d)**. While most cristae are orthogonal to the OMM, we observed a wide range of CJ angles in s-Opa1* mitochondria. Overall, the CJ angles in s-Opa1* cristae are less perpendicular compared to WT CJs, demonstrating that the tilted cristae observed in these cells occurs at the CJ (**Fig. 2a and 3b-c**).

We also found that some cristae have two or more CJs. Most l-Opa1* mitochondria (77%) have at least one crista with multiple junctions, which is considerably higher than WT (35%), Opa1-OE (30%), s-Opa1* (27%), and Opa1-KO (25%) mitochondria (**Fig. S8a**). These multijunction cristae were further classified as straight or loop. In WT cells, there is an equivalent number of straight and loop cristae with more than one CJ and in Opa1-KO mitochondria, the ratio shifts to favor the loop class (**Fig S8b**). In Opa1-OE and l-Opa1* mitochondria, the majority of multijunction cristae fall into the straight category, correlating with a greater proportion of straight-across cristae shapes observed in l-Opa1* mitochondria (**Fig. 3b and S8b**).

Functional consequences of Opa1 state

We next examined the consequences of Opa1 levels and processing on mitochondrial function. First, we sought to uncover potential effects of Opa1 perturbation on the intrinsic apoptotic pathway. We used BH3 profiling to compare mitochondrial responses to pro-apoptotic stimuli across the cell lines. BH3

profiling quantifies the percentage of cells that release cytochrome c from their mitochondria, the key commitment step in mitochondrial apoptosis, in response to treatment with BH3 peptides that mimic the activity of pro-apoptotic proteins from the BCL-2 family (Fraser *et al*, 2018). Cells that release cytochrome c in response to moderate or weak pro-apoptotic stimuli are considered to be primed for apoptosis, whereas cells that require strong stimuli to trigger cytochrome c release are unprimed. Apoptotic priming has been previously shown to determine whether healthy and cancerous cells undergo apoptosis in response to cellular stress or damage (Chonghaile *et al*, 2011; Sarosiek *et al*, 2017; Spetz *et al*, 2022). BH3 profiling showed a substantial reduction in apoptotic priming of Opa1-KO cells relative to WT cells as indicated by decreased sensitivity to the BIM BH3 peptide, which can inhibit all pro-survival Bcl-2 family proteins and directly activate BAX and BAK (Kale *et al*, 2018) (**Fig. 4a**). Equal doses of the BIM BH3 peptide induced less cytochrome c release from mitochondria in Opa1-KO cells than WT cells, indicating that stronger pro-death stimuli are required to induce apoptosis in cells lacking Opa1 (**Fig. 4a**). We also tested MEF sensitivity to common apoptosis-inducing agents by quantifying positivity for Annexin V, which binds phosphatidylserine on the surface of cells undergoing early apoptosis, after treatment. Based on the BH3 profiling results, we would expect less apoptosis after treatment of Opa1-KO cells than WT cells. We found that indeed this was the case: Opa1-KO MEF were more resistant to treatment with the topoisomerase inhibitor etoposide, DNA damaging agent doxorubicin, and pan-kinase inhibitor staurosporine at 24 hours (**Fig. 4b**). Similar differences in sensitivity were also detected at 48 and 72 hours, suggesting that retention of cytochrome c durably protected Opa1 KO cells from commitment to apoptosis (**Fig. S9**). Overexpression of Opa1 maintains a WT-level response to apoptotic stimuli. While s-Opa1* cells show levels of apoptotic priming between WT and Opa1-KO cells, the short-form is not sufficient to rescue normal apoptotic priming of MEF. In contrast, l-Opa1* cells behave similarly to the WT cells across most conditions, restoring apoptotic priming (**Fig. 4a**). These results suggest that these lines would not be as resistant to apoptosis-inducing agents as the Opa1-KO cells and is evident in the 24-hour chemosensitivity data for etoposide, doxorubicin, and staurosporine treatment (**Fig. 4b**) as well as data at 48- and 72-hours post-treatment (**Fig. S9**). The presence of a stable l-Opa1 population has been previously shown to be essential in apoptotic resistance (Merkwirth *et al*, 2008, 2012). Our results indicate Opa1 processing is not required for apoptotic priming. In Opa1-KO or s-Opa1* cells, wider CJ at steady-state conditions correlated with cells resistant to apoptosis.

To understand the impact of Opa1-dependent remodeling on mitochondrial calcium homeostasis and mitochondrial permeability transition pore (mPTP) opening, we performed mitochondrial calcium retention capacity (CRC) assay on MEF cell lines. Mitochondria from permeabilized l-Opa1* cells show similar CRC profiles to WT **(Fig. 4c)**. In contrast, s-Opa1* cells and Opa1-KO cells are observed to be more resistant to mPTP opening **(Fig. 4c)** and require higher concentrations of $CaCl_2$ to induce the pore

opening transition **(Fig. 4b)**. The presence of vesicular cristae and wider CJs at steady-state conditions correlate with s-Opa1* and Opa1-KO cells resistant to calcium-induced mPTP opening. In contrast, Opa1-OE cells undergo mPTP transition at lower amounts of $CaCl_2$ stimulation. We note an elevated presence of mitochondrial calcium deposits in the Opa1-OE cell line **(Fig. S3H)**.

Next, we evaluated the mitochondrial respiratory fitness of all cell lines to assess how a key cristae-dependent function varies upon Opa1 perturbation. As previously observed, mitochondrial respiration is severely impaired in Opa1-KO cells (Zhang *et al*, 2011) (**Fig. 5a**). Basal OCR levels for Opa1-OE cells are similar to WT. s-Opa1* and l-Opa1* cells both have basal oxygen consumption respiration (OCR) levels significantly lower than WT, as previously reported (Lai *et al*, 2020; Lee *et al*, 2020). Cell lines with lower basal OCRs, also display significantly lower maximal respiration and spare capacity levels. Longer cristae and more amorphous cristae were observed in these cell lines. These results suggest that balanced levels of both forms of Opa1 are required for normal mitochondrial respiration.

Mitochondrial fitness was also measured in the $Oma1^{-/-}$ background in which the l-Opa1* cells were generated (Wang *et al*, 2021). Like l-Opa1* cells, $Oma1^{-/-}$ cells also have WT levels of cytochrome c release upon treatment with BIM **(Fig S10a)**. Additionally, $Oma1^{-/-}$ MEF cells show WT-like propensity for mPTP opening under Ca^{2+} stimulation albeit displaying a lower overall calcium buffering profile than WT and l-Opa1* cells **(Fig S10b)**. OCR values in l-Opa1* cells are significantly lower than in $Oma1^{-/-}$ cells, indicating the *oma1* deletion is not the sole contributor to the impaired respiration observed in l-Opa1* cells **(Fig. S10c-d)**. These data suggest that functional differences in the l-Opa1* mitochondria are dependent on the form of Opa1 present.

Finally, we investigated the effect of Opa1 imbalance on mtDNA maintenance. Mitochondrial fusion is essential for maintaining mtDNA stability (Elachouri *et al*, 2011) and Opa1 depletion has been shown to lead to a decrease in mtDNA number and translation (Chen *et al*, 2010). Consistent with previous reports, we observed robust mtDNA decrease in Opa1-KO MEF quantified by instant Structured Illumination Microscopy (iSIM) imaging **(Fig. S11a-c)** and qPCR **(Fig. S11d)**. Stimulated emission depletion (STED) microscopy studies in HeLa and human fibroblast cells have shown that nucleoids occupy mitochondrial matrix spaces between clusters of cristae (Stephan *et al*, 2019) and when fusion is inhibited, nucleoids cluster without changes in size and copy number (Ramos *et al*, 2019). We observed higher nucleoid area and puncta in l-Opa1* cells than in WT cells **(Fig. S11b-c)**. No difference in mtDNA copy number was observed in l-Opa1* cells by qPCR **(Fig. S11d)**, suggesting these changes are likely due to mtDNA distribution and organization.

Discussion

Understanding how sophisticated membrane architectures are generated in pleiomorphic organelles poses a challenge and opportunity for structural cell biology. The mitochondrion is an exemplar case where the organelle's morphology can take on a wide range of forms regulated by dynamic protein assemblies (Mageswaran *et al*, 2023). In this work, we used state-of-the-art *in situ* cryo-ET to analyze how Opa1 processing regulates mitochondrial ultrastructure, in particular cristae morphology. Previous analyses of mitochondrial cristae morphology have been informed by conventional TEM micrographs of fixed and heavy metal-stained cells known to perturb membrane structures and introduce imaging artifacts (Scorrano *et al*, 2002; Olichon *et al*, 2003; Frezza *et al*, 2006). In overcoming these limitations, we characterized and quantified a diverse range of cristae morphologies specific to the form of Opa1 present in the cell. Here, we discuss structure/function relationships which emerged from this study (**Fig. 6**).

Our 3D data captures the diversity of cristae morphologies and can distinguish lamellar and tubular cristae. While the majority of cristae are lamellar, tubular cristae were observed in WT mitochondria and a fraction of s-Opa1* cells, but are entirely absent from l-Opa1* cells (**Fig. 2a, b, e; Fig. 6a, b**). Tubular cristae are compatible with reported *in vitro* helical assemblies of the yeast homolog, s-Mgm1 reconstituted on membranes (Faelber *et al*, 2019). Recent single particle cryo-EM helical reconstructions of human s-Opa1 decorating the exterior of membranes tubes show how paddle domain interactions facilitate self-assembly (Malsburg *et al*, 2023; Nyenhuis *et al*, 2023). The increase in globular cristae in the Opa1-KO condition may imply that the presence of either or both forms of Opa1 support lamellar cristae. Indeed, a recent study found knock-down of Opa1 altered the ratio of lamellar to tubular cristae (Suga *et al*, 2023). Stacking cristae phenotype in l-Opa1* as well as increased presence of multijunction cristae may implicate an accumulation of fusion intermediates (**Fig. 6c**). Further integrative structural studies will also be necessary to directly relate how specific protein conformational states influence such morphologies (**Fig. 6c**) (Harner *et al*, 2016).

Visualizing mitochondrial membrane structure using cryo-ET enables us to make accurate measurements of membrane distances. l-Opa1* cells maintained WT-like CJ widths (**Fig. 3a**), which with our BH3 profiling assay suggest that l-Opa1 plays a role in maintaining CJ widths and mediating the response to apoptotic stimulation (**Fig. 6d**). TEM imaging showed that cytochrome c release (stimulated by pro-apoptotic signaling proteins such as BID) results in the widening of cristae junctions and opening of the cristae lumen (Scorrano *et al*, 2002; Frezza *et al*, 2006). In contrast to previous studies, we investigated cristae state prior to any exposure to extracellular stress or apoptotic stimuli (Merkwirth *et al*, 2008, 2012). Building upon previous studies, we observed wider cristae junctions in Opa1-KO and s-Opa1* cells prior to apoptotic initiation (**Fig. 3**). Together, with our apoptotic priming results demonstrating

that cells lacking l-Opa1 released less cytochrome c upon apoptosis stimulation, our observations support a specific CJ regulatory role for l-Opa1 in the cytochrome c release transition (**Fig. 6b, c**) (Merkwirth *et al*, 2008).

Our findings that Opa1-KO cells are resistant to apoptosis may seem counterintuitive given previous reports of apoptotic resistance in Opa1-overexpressing cells (Frezza *et al*, 2006)**.** However, this apparent discrepancy can be reconciled if considering multiple roles for Opa1 during apoptotic membrane transitions. During apoptosis, Opa1 maintains cristae junctions, which may restrict cytochrome c release in response to pro-apoptotic signals (Frezza *et al*, 2006). However, the importance of rearrangement and disassembly of Opa1 complexes during apoptosis initiation, to facilitate CJ opening, as discussed above, demonstrates that Opa1 also has a direct role in the earlier steps when apoptosis is being initiated (**Fig. 6d**). This view is consistent with our finding that complete knock-out of Opa1 impairs cytochrome c release and can be protective against apoptosis-inducing agents (**Fig. 4a-b**). Our data indicate that apoptotic response is independent of Opa1 processing (Cipolat *et al*, 2006) and cytochrome c release is dependent on initial CJ widths.

Our BH3 profiling results are supported by CRC assay results, where l-Opa1 presence in MEF allows for WT-like responses towards increased Ca^{2+} and apoptotic stimulation (**Fig. 4c-d**). These independent functional outcomes are connected by the importance of membrane integrity in mPTP opening (Strubbe-Rivera *et al*, 2021; Bernardi *et al*, 2023) and BAX/BAK-mediated cytochrome c cristae remodeling (Scorrano *et al*, 2002; Renault *et al*, 2015). Consistent with previous reports of calcium phosphate deposits, we observed dense deposits in the mitochondria matrix of most Opa1-OE mitochondria (Wolf *et al*, 2017), which correlates with a lower mPTP transition $CaCl_2$ threshold. Cryo-ET enabled this finding and allows us to attribute differences in density in the mitochondrial matrix to biological material, and not artifacts from chemical agents. We note a less condensed matrix in mitochondria in s-Opa1* cells and a lighter matrix in the Opa1-KO mitochondria, which we speculate may be related to matrix components other than calcium.

Our measurements also suggest that l-Opa1 may contribute to maintaining perpendicular CJ, as fewer perpendicular CJs were observed in s-Opa1* cells. Perpendicular CJs can facilitate cristae stacking, which we noticed in a striking number of l-Opa1* cells. Stacking cristae have been previously observed both under conditions that induce metabolic and endoplasmic reticulum stress upon addition of thapsigargin (Barad *et al*, 2022) and in $Oma1^{-/-}$ cells (Anand *et al*, 2014). We speculate that cristae stacking may have features in common to an intermediate preceding fusion (**Fig. 6c**). Consistent with this role, we also note a correlation between stacked cristae organization in the l-Opa1* cells facilitating mtDNA distribution. While Opa1-KO cells have a dramatic loss of mtDNA number, we still visualize the

presence of cristae in these mitochondria. This further supports emerging evidence that the organization of multiple crista contribute to mtDNA maintenance (Stephan *et al*, 2019; Jakubke *et al*, 2021).

We also assessed the effects of Opa1 state on mitochondrial respiration, a central function dependent on cristae shape (Cogliati *et al*, 2016). In short, compromised respiration observed in l-Opa1*, s-Opa1*, and Opa1-KO cells correlates with a larger percentage of amorphous cristae and longer cristae lengths. This suggests both forms of Opa1 play a role in maintaining a defined cristae shape and length. Our work indicates more subtle cristae phenotypes (such as vesicular and amorphous) may also not be optimal for respiration (**Fig. 6**). We speculate disruption of cristae shape could destabilize respiratory complex assembly in the cristae membranes or vice versa. Future studies will be necessary to more directly link *in situ* mitochondrial ultrastructure with mitochondrial dysfunction.

In summary, here we characterize cristae morphologies related to the levels or forms of Opa1 present in the cell. We characterize and quantify cristae morphological differences and define distinct differences specific to each Opa1 form. Notably, we find evidence that l-Opa1 plays important roles in maintaining CJ width and connectivity, which correlates well with WT-like apoptotic and calcium responses. We also demonstrate that both forms of Opa1 are required for maintaining cristae membrane shape and mitochondrial respiration, linking amorphous cristae with mitochondrial dysfunction. This work, in describing cristae morphology and functions, opens new opportunities for understanding mitochondrial ultrastructure and function, and motivates further studies visualizing and dissecting mechanisms underlying cristae heterogeneity by new live cell imaging approaches to gain insights into the spatio-temporal regulation of their lifecycle.

Acknowledgments

We are grateful to Christopher Borsa, Phat Vinh Dip, and Edward Brignole at the MIT.nano cryo-EM facility and Kang Song and Chen Xu at the University of Massachusetts cryo-EM facility for providing access to the cryo-EM microscopes and for all their help, advice, and maintenance of cryo-EM equipment. Electron microscopy was performed in the Microscopy Core of the Center for Systems Biology/Program in Membrane Biology, which is partially supported by an Inflammatory Bowel Disease Grant DK043351 and a Boston Area Diabetes and Endocrinology Research Center (BADERC) Award DK057521. We thank Connor Tou for assistance cloning guide RNAs. We thank Dr Patrick Ward and Dr Owen Skinner for helpful discussions, and the laboratories of Dr Vamsi Mootha and Dr Joshua Kaplan at Department of Molecular Biology, MGH for equipment access and support.

Grants/funding:

M.Y.F. is a Fellow of The Jane Coffin Childs Fund for Medical Research. P.P.N. was supported by the Swiss National Science Foundation (SNSF) Early Postdoc.Mobility P2BSP3_188112 and Postdoc.Mobility P400PB_199252 fellowships. Z.I. was supported by NIA award F32AG077861. This work was supported by a Mass General Hospital ECOR Howard M. Goodman Fellowship (to B.P.K.); Charles H. Hood Foundation Child Health Research Awards to L.H.C. and K.A.S.; and Alex's Lemonade Stand Foundation for Childhood Cancers Research Award to K.A.S. This work was supported by funding from the National Institutes of Health (R01DK125263 and R37CA248565 to K.A.S.; R35GM142553 to L.H.C.).

Author Contributions

Michelle Y. Fry, Conceptualization; funding acquisition, data curation; investigation; formal analysis; software; validation; visualization; methodology; writing – original draft; writing – review and editing. **Paula P. Navarro**: Conceptualization; supervision, funding acquisition, data curation; investigation; formal analysis; validation; visualization; methodology; writing – original draft; writing – review and editing. **Pusparanee Hakim**: Data curation; investigation; formal analysis; validation; visualization; methodology; writing – original draft; writing – review and editing. **Virly Y. Ananda**: Data curation; software; formal analysis; validation; visualization; methodology; writing – original draft; writing – review and editing. **Xingping Qin**: Data curation; investigation; formal analysis; validation; writing – review and editing. **Juan C. Landoni**: Data curation; investigation; formal analysis; validation; writing – review and editing. **Sneha Rath**: Data curation; investigation; formal analysis; validation; writing – review and editing. **Zintis Inde**: Data curation; investigation; writing – review and editing. **Camila Makhlouta Lugo**: Data curation; formal analysis; validation; visualization; methodology; writing – review and editing. **Bridget E. Luce**: Formal

analysis; visualization; writing – original draft; writing – review and editing. **Yifan Ge:** Conceptualization**;** Data curation; investigation; writing – review and editing. **Julie L. McDonald**: Data curation; investigation; writing – review and editing. **Ilzat Ali**: Formal analysis; software; visualization. **Leillani L. Ha**: Methodology; investigation; formal analysis. **Benjamin P. Kleinstiver**: Supervision; funding acquisition; writing – review and editing. **David C. Chan**: Resources, writing – review and editing. **Kristopher A. Sarosiek**: Supervision; funding acquisition; writing – original draft; writing – review and editing. **Luke H. Chao**: Conceptualization; supervision; project administration; funding acquisition; visualization; methodology; writing – original draft; writing – review and editing.

Declaration of Interests

B.P.K is an inventor on patents and/or patent applications filed by Mass General Brigham that describe genome engineering technologies. B.P.K. is a consultant for EcoR1 capital, and is an advisor to Acrigen Biosciences, Life Edit Therapeutics, and Prime Medicine. L.H.C. is an advisor for Stealth Biotherapeutics. The remaining authors declare that there are no competing financial interests.

References

Anand R, Wai T, Baker MJ, Kladt N, Schauss AC, Rugarli E & Langer T (2014) The i-AAA protease YME1L and OMA1 cleave OPA1 to balance mitochondrial fusion and fission. *J Cell Biol* 204: 919–929

Barad BA, Medina M, Fuentes D, Wiseman RL & Grotjahn DA (2022) A surface morphometrics toolkit to quantify organellar membrane ultrastructure using cryo-electron tomography. *Biorxiv*: 2022.01.23.477440

Bäuerlein FJB & Baumeister W (2021) Towards Visual Proteomics at High Resolution. *J Mol Biol* 433: 167187

Bepler T, Kelley K, Noble AJ & Berger B (2020) Topaz-Denoise: general deep denoising models for cryoEM and cryoET. *Nat Commun* 11: 5208

Bernardi P, Gerle C, Halestrap AP, Jonas EA, Karch J, Mnatsakanyan N, Pavlov E, Sheu S-S & Soukas AA (2023) Identity, structure, and function of the mitochondrial permeability transition pore: controversies, consensus, recent advances, and future directions. *Cell Death Differ*: 1–17

Blum TB, Hahn A, Meier T, Davies KM & Kühlbrandt W (2019) Dimers of mitochondrial ATP synthase induce membrane curvature and self-assemble into rows. *Proc National Acad Sci* 116: 4250–4255

Bocca C, Kane MS, Veyrat-Durebex C, Chupin S, Alban J, Nzoughet JK, Mao ML, Barca JMC de la, Amati-Bonneau P, Bonneau D, *et al* (2018) The Metabolomic Bioenergetic Signature of Opa1-Disrupted Mouse Embryonic Fibroblasts Highlights Aspartate Deficiency. *Sci Rep-uk* 8: 11528

455 Castaño-Díez D, Kudryashev M, Arheit M & Stahlberg H (2012) Dynamo: A flexible, user-friendly
456 development tool for subtomogram averaging of cryo-EM data in high-performance computing
457 environments. *J Struct Biol* 178: 139–151

458 Chandel NS (2014) Mitochondria as signaling organelles. *Bmc Biol* 12: 34

459 Chen H, Vermulst M, Wang YE, Chomyn A, Prolla TA, McCaffery JM & Chan DC (2010) Mitochondrial
460 Fusion Is Required for mtDNA Stability in Skeletal Muscle and Tolerance of mtDNA Mutations. *Cell*
461 141: 280–289

462 Chonghaile TN, Sarosiek KA, Vo T-T, Ryan JA, Tammareddi A, Moore VDG, Deng J, Anderson KC,
463 Richardson P, Tai Y-T, *et al* (2011) Pretreatment Mitochondrial Priming Correlates with Clinical
464 Response to Cytotoxic Chemotherapy. *Science* 334: 1129–1133

465 Cipolat S, Rudka T, Hartmann D, Costa V, Serneels L, Craessaerts K, Metzger K, Frezza C, Annaert W,
466 D'Adamio L, *et al* (2006) Mitochondrial Rhomboid PARL Regulates Cytochrome c Release during
467 Apoptosis via OPA1-Dependent Cristae Remodeling. *Cell* 126: 163–175

468 Cogliati S, Enriquez JA & Scorrano L (2016) Mitochondrial Cristae: Where Beauty Meets Functionality.
469 *Trends Biochem Sci* 41: 261–273

470 Czech E, Aksoy BA, Aksoy P & Hammerbacher J (2019) Cytokit: a single-cell analysis toolkit for high
471 dimensional fluorescent microscopy imaging. *BMC Bioinform* 20: 448

472 Elachouri G, Vidoni S, Zanna C, Pattyn A, Boukhaddaoui H, Gaget K, Yu-Wai-Man P, Gasparre G, Sarzi
473 E, Delettre C, *et al* (2011) OPA1 links human mitochondrial genome maintenance to mtDNA
474 replication and distribution. *Genome Res* 21: 12–20

475 Faelber K, Dietrich L, Noel JK, Wollweber F, Pfitzner A-K, Mühleip A, Sánchez R, Kudryashev M,
476 Chiaruttini N, Lilie H, *et al* (2019) Structure and assembly of the mitochondrial membrane remodelling
477 GTPase Mgm1. *Nature* 571: 429–433

478 Fraser C, Ryan J & Sarosiek K (2018) BH3 Profiling: A Functional Assay to Measure ApoptoticPriming
479 and Dependencies. *Methods Mol Biology* 1877: 61–76

480 Fraser CS, Spetz JKE, Qin X, Presser A, Choiniere J, Li C, Yu S, Blevins F, Hata AN, Miller JW, *et al*
481 (2022) Exploiting endogenous and therapy-induced apoptotic vulnerabilities in immunoglobulin light
482 chain amyloidosis with BH3 mimetics. *Nat Commun* 13: 5789

483 Frey TG & Mannella CA (2000) The internal structure of mitochondria. *Trends Biochem Sci* 25: 319–324

484 Frezza C, Cipolat S, Brito OM de, Micaroni M, Beznoussenko GV, Rudka T, Bartoli D, Polishuck RS,
485 Danial NN, Strooper BD, *et al* (2006) OPA1 Controls Apoptotic Cristae Remodeling Independently
486 from Mitochondrial Fusion. *Cell* 126: 177–189

487 Friedman JR & Nunnari J (2014) Mitochondrial form and function. *Nature* 505: 335–343

488 Ge Y, Shi X, Boopathy S, McDonald J, Smith AW & Chao LH (2020) Two forms of Opa1 cooperate to
489 complete fusion of the mitochondrial inner-membrane. *Elife* 9: e50973

490 Hagen WJH, Wan W & Briggs JAG (2017) Implementation of a cryo-electron tomography tilt-scheme
491 optimized for high resolution subtomogram averaging. *J Struct Biol* 197: 191–198

492 Harner ME, Unger A-K, Geerts WJ, Mari M, Izawa T, Stenger M, Geimer S, Reggiori F, Westermann B
493 & Neupert W (2016) An evidence based hypothesis on the existence of two pathways of mitochondrial
494 crista formation. *Elife* 5: e18853

495 Hashimi H (2019) A parasite's take on the evolutionary cell biology of MICOS. *Plos Pathog* 15: e1008166

496 Jakubke C, Roussou R, Maiser A, Schug C, Thoma F, Bunk D, Hörl D, Leonhardt H, Walter P, Klecker
497 T, *et al* (2021) Cristae-dependent quality control of the mitochondrial genome. *Sci Adv* 7: eabi8886

498 Kale J, Osterlund EJ & Andrews DW (2018) BCL-2 family proteins: changing partners in the dance
499 towards death. *Cell Death Differ* 25: 65–80

500 Kremer JR, Mastronarde DN & McIntosh JR (1996) Computer Visualization of Three-Dimensional Image
501 Data Using IMOD. *J Struct Biol* 116: 71–76

502 Laan M van der, Horvath SE & Pfanner N (2016) Mitochondrial contact site and cristae organizing system.
503 *Curr Opin Cell Biol* 41: 33–42

504 Lai Y, Lin P, Chen M, Zhang Y, Chen J, Zheng M, Liu J, Du H, Chen R, Pan X, *et al* (2020) Restoration
505 of L-OPA1 alleviates acute ischemic stroke injury in rats via inhibiting neuronal apoptosis and
506 preserving mitochondrial function. *Redox Biol* 34: 101503

507 Lee H, Smith SB, Sheu S-S & Yoon Y (2020) The short variant of optic atrophy 1 (OPA1) improves cell
508 survival under oxidative stress. *J Biol Chem* 295: 6543–6560

509 Mageswaran SK, Grotjahn DA, Zeng X, Barad BA, Medina M, Hoang MH, Dobro MJ, Chang Y-W, Xu M,
510 Yang WY, *et al* (2023) Nanoscale details of mitochondrial constriction revealed by cryo-electron
511 tomography. *Biophys J*

512 Mahamid J, Pfeffer S, Schaffer M, Villa E, Danev R, Cuellar LK, Förster F, Hyman AA, Plitzko JM &
513 Baumeister W (2016) Visualizing the molecular sociology at the HeLa cell nuclear periphery. *Science*
514 351: 969–972

515 Mahecic D, Gambarotto D, Douglass KM, Fortun D, Banterle N, Ibrahim KA, Guennec ML, Gönczy P,
516 Hamel V, Guichard P, *et al* (2020) Homogeneous multifocal excitation for high-throughput super-
517 resolution imaging. *Nat Methods* 17: 726–733

518 Malsburg A von der, Sapp GM, Zuccaro KE, Appen A von, Moss FR, Kalia R, Bennett JA, Abriata LA,
519 Peraro MD, Laan M van der, *et al* (2023) Structural mechanism of mitochondrial membrane
520 remodelling by human OPA1. *Nature*: 1–8

521 Mannella CA (2006) Structure and dynamics of the mitochondrial inner membrane cristae. *Biochimica Et*
522 *Biophysica Acta Bba - Mol Cell Res* 1763: 542–548

523 Martinez-Sanchez A, Garcia I, Asano S, Lucic V & Fernandez J-J (2014) Robust membrane detection
524 based on tensor voting for electron tomography. *J Struct Biol* 186: 49–61

525 Mastronarde DN (2003) SerialEM: A Program for Automated Tilt Series Acquisition on Tecnai
526 Microscopes Using Prediction of Specimen Position. *Microsc Microanal* 9: 1182–1183

527 Mastronarde DN & Held SR (2017) Automated tilt series alignment and tomographic reconstruction in
528 IMOD. *J Struct Biol* 197: 102–113

529 Merkwirth C, Dargazanli S, Tatsuta T, Geimer S, Löwer B, Wunderlich FT, Kleist-Retzow J-C von,
530 Waisman A, Westermann B & Langer T (2008) Prohibitins control cell proliferation and apoptosis by
531 regulating OPA1-dependent cristae morphogenesis in mitochondria. *Gene Dev* 22: 476–488

532 Merkwirth C, Martinelli P, Korwitz A, Morbin M, Brönneke HS, Jordan SD, Rugarli EI & Langer T (2012)
533 Loss of Prohibitin Membrane Scaffolds Impairs Mitochondrial Architecture and Leads to Tau
534 Hyperphosphorylation and Neurodegeneration. *Plos Genet* 8: e1003021

535 Mishra P, Carelli V, Manfredi G & Chan DC (2014) Proteolytic Cleavage of Opa1 Stimulates Mitochondrial
536 Inner Membrane Fusion and Couples Fusion to Oxidative Phosphorylation. *Cell Metab* 19: 630–641

537 Mishra P & Chan DC (2016) Metabolic regulation of mitochondrial dynamics. *J Cell Biol* 212: 379–387

538 Navarro P, Scaramuzza S, Stahlberg H & Castaño-Díez D (2020) The Dynamo Software Package for
539 Cryo-electron Tomography and Subtomogram Averaging. *Microsc Microanal* 26: 3142–3145

540 Navarro PP (2022) Quantitative Cryo-Electron Tomography. *Frontiers Mol Biosci* 9: 934465

541 Navarro PP, Stahlberg H & Castaño-Díez D (2018) Protocols for Subtomogram Averaging of Membrane
542 Proteins in the Dynamo Software Package. *Frontiers Mol Biosci* 5: 82

543 Navarro PP, Vettiger A, Ananda VY, Llopis PM, Allolio C, Bernhardt TG & Chao LH (2022) Cell wall
544 synthesis and remodelling dynamics determine division site architecture and cell shape in Escherichia
545 coli. *Nat Microbiol* 7: 1621–1634

546 Nyenhuis SB, Wu X, Strub M-P, Yim Y-I, Stanton AE, Baena V, Syed ZA, Canagarajah B, Hammer JA &
547 Hinshaw JE (2023) OPA1 helical structures give perspective to mitochondrial dysfunction. *Nature*: 1–
548 9

549 Olichon A, Baricault L, Gas N, Guillou E, Valette A, Belenguer P & Lenaers G (2003) Loss of OPA1
550 Perturbates the Mitochondrial Inner Membrane Structure and Integrity, Leading to Cytochrome c
551 Release and Apoptosis*. *J Biol Chem* 278: 7743–7746

552 Patten DA, Wong J, Khacho M, Soubannier V, Mailloux RJ, Pilon-Larose K, MacLaurin JG, Park DS,
553 McBride HM, Trinkle-Mulcahy L, *et al* (2014) OPA1-dependent cristae modulation is essential for
554 cellular adaptation to metabolic demand. *Embo J* 33: 2676–2691

555 Pettersen EF, Goddard TD, Huang CC, Couch GS, Greenblatt DM, Meng EC & Ferrin TE (2004) UCSF
556 Chimera—A visualization system for exploratory research and analysis. *J Comput Chem* 25: 1605–
557 1612

558 Picard M & Shirihai OS (2022) Mitochondrial signal transduction. *Cell Metab* 34: 1620–1653

559 Ramos ES, Motori E, Brüser C, Kühl I, Yeroslaviz A, Ruzzenente B, Kauppila JHK, Busch JD, Hultenby
560 K, Habermann BH, *et al* (2019) Mitochondrial fusion is required for regulation of mitochondrial DNA
561 replication. *PLoS Genet* 15: e1008085

562 Renault TT, Floros KV, Elkholi R, Corrigan K-A, Kushnareva Y, Wieder SY, Lindtner C, Serasinghe MN,
563 Asciolla JJ, Buettner C, *et al* (2015) Mitochondrial Shape Governs BAX-Induced Membrane
564 Permeabilization and Apoptosis. *Mol Cell* 57: 69–82

565 Rigort A, Bäuerlein FJB, Villa E, Eibauer M, Laugks T, Baumeister W & Plitzko JM (2012) Focused ion
566 beam micromachining of eukaryotic cells for cryoelectron tomography. *Proc National Acad Sci* 109:
567 4449–4454

568 Sarosiek KA, Fraser C, Muthalagu N, Bhola PD, Chang W, McBrayer SK, Cantlon A, Fisch S, Golomb-
569 Mello G, Ryan JA, *et al* (2017) Developmental Regulation of Mitochondrial Apoptosis by c-Myc
570 Governs Age- and Tissue-Specific Sensitivity to Cancer Therapeutics. *Cancer Cell* 31: 142–156

571 Schägger H & Pfeiffer K (2000) Supercomplexes in the respiratory chains of yeast and mammalian
572 mitochondria. *Embo J* 19: 1777–1783

573 Schindelin J, Arganda-Carreras I, Frise E, Kaynig V, Longair M, Pietzsch T, Preibisch S, Rueden C,
574 Saalfeld S, Schmid B, *et al* (2012) Fiji: an open-source platform for biological-image analysis. *Nat*
575 *Methods* 9: 676–682

576 Scorrano L, Ashiya M, Buttle K, Weiler S, Oakes SA, Mannella CA & Korsmeyer SJ (2002) A Distinct
577 Pathway Remodels Mitochondrial Cristae and Mobilizes Cytochrome c during Apoptosis. *Dev Cell* 2:
578 55–67

579 Singh R, Yu S, Osman M, Inde Z, Fraser C, Cleveland AH, Almanzar N, Lim CB, Joshi GN, Spetz J, *et*
580 *al* (2023) Radiation therapy-induced neurocognitive impairment is driven by heightened apoptotic
581 priming in early life and prevented by blocking BAX. *Cancer Res*: OF1–OF20

582 Song Z, Chen H, Fiket M, Alexander C & Chan DC (2007) OPA1 processing controls mitochondrial fusion
583 and is regulated by mRNA splicing, membrane potential, and Yme1L. *J Cell Biology* 178: 749–755

584 Spetz JKE, Florido MHC, Fraser CS, Qin X, Choiniere J, Yu SJ, Singh R, Friesen M, Rubin LL, Salem J-
585 E, *et al* (2022) Heightened apoptotic priming of vascular cells across tissues and life span predisposes
586 them to cancer therapy–induced toxicities. *Sci Adv* 8: eabn6579

587 Spinelli JB & Haigis MC (2018) The multifaceted contributions of mitochondria to cellular metabolism.
588 *Nat Cell Biol* 20: 745–754

589 Stephan T, Roesch A, Riedel D & Jakobs S (2019) Live-cell STED nanoscopy of mitochondrial cristae.
590 *Sci Rep-uk* 9: 12419

591 Strubbe-Rivera JO, Schrad JR, Pavlov EV, Conway JF, Parent KN & Bazil JN (2021) The mitochondrial
592 permeability transition phenomenon elucidated by cryo-EM reveals the genuine impact of calcium
593 overload on mitochondrial structure and function. *Sci Rep-uk* 11: 1037

Suga S, Nakamura K, Nakanishi Y, Humbel BM, Kawai H & Hirabayashi Y (2023) An interactive deep learning-based approach reveals mitochondrial cristae topologies. *PLOS Biol* 21: e3002246

Turoňová B, Schur FKM, Wan W & Briggs JAG (2017) Efficient 3D-CTF correction for cryo-electron tomography using NovaCTF improves subtomogram averaging resolution to 3.4Å. *J Struct Biol* 199: 187–195

Twig G, Elorza A, Molina AJA, Mohamed H, Wikstrom JD, Walzer G, Stiles L, Haigh SE, Katz S, Las G, *et al* (2008) Fission and selective fusion govern mitochondrial segregation and elimination by autophagy. *Embo J* 27: 433–446

Wagner FR, Watanabe R, Schampers R, Singh D, Persoon H, Schaffer M, Fruhstorfer P, Plitzko J & Villa E (2020) Preparing samples from whole cells using focused-ion-beam milling for cryo-electron tomography. *Nat Protoc* 15: 2041–2070

Walton RT, Christie KA, Whittaker MN & Kleinstiver BP (2020) Unconstrained genome targeting with near-PAMless engineered CRISPR-Cas9 variants. *Science* 368: 290–296

Wang R, Mishra P, Garbis SD, Moradian A, Sweredoski MJ & Chan DC (2021) Identification of new OPA1 cleavage site reveals that short isoforms regulate mitochondrial fusion. *Mol Biol Cell* 32: 157–168

Wolf SG, Mutsafi Y, Dadosh T, Ilani T, Lansky Z, Horowitz B, Rubin S, Elbaum M & Fass D (2017) 3D visualization of mitochondrial solid-phase calcium stores in whole cells. *Elife* 6: e29929

Wolff G, Limpens RWAL, Zheng S, Snijder EJ, Agard DA, Koster AJ & Bárcena M (2019) Mind the gap: Micro-expansion joints drastically decrease the bending of FIB-milled cryo-lamellae. *J Struct Biol* 208: 107389

York AG, Chandris P, Nogare DD, Head J, Wawrzusin P, Fischer RS, Chitnis A & Shroff H (2013) Instant super-resolution imaging in live cells and embryos via analog image processing. *Nat Methods* 10: 1122–1126

Zhang Z, Wakabayashi N, Wakabayashi J, Tamura Y, Song W-J, Sereda S, Clerc P, Polster BM, Aja SM, Pletnikov MV, *et al* (2011) The dynamin-related GTPase Opa1 is required for glucose-stimulated ATP production in pancreatic beta cells. *Mol Biol Cell* 22: 2235–2245

Zick M, Rabl R & Reichert AS (2009) Cristae formation—linking ultrastructure and function of mitochondria. *Biochimica Et Biophysica Acta Bba - Mol Cell Res* 1793: 5–19

Methods

Cell lines and culture

MEF were maintained in DMEM supplemented with 10% fetal bovine serum (FBS) and 1% penicillin/streptomycin at 37°C and 5% CO_2. Wildtype and Opa1 knock-out MEF cell lines were purchased

from ATCC. *⊿exon5b/Oma1*$^{-/-}$ cells and Opa1 knock-outs transfected retrovirally with Opa1 Isoform 5 (KO Opa1 + Iso5) were kind gifts from David Chan (California Institute of Technology) (Song *et al*, 2007). The KO Opa1 + Iso5 were maintained in the same condition described above and supplemented with puromycin at 1 µg/mL. Cell genotypes were confirmed by Western blotting. To mediate a constitutive overexpression of Opa1 from the safe harbor locus Rosa26 in MEF, mouse Opa1 sequence was cloned into pR26-CMVconst (Addgene plasmid #127373; http://n2t.net/addgene:127373; RRID: Addgene_127373; kind gift by Lance Miller) to generate pR26-CMV-Opa1 (pAH33). Following sequence verification, the construct was co-transfected with pX330-sgR26 (Addgene plasmid #127376; http://n2t.net/addgene:127376; RRID: Addgene_127376; kind gift by Lance Miller) into WT MEF cells using Lipofectamine 3000. Transfected cells were selected with 5 µg/mL puromycin starting 24 hours post-transfection for 7 days. Stable clones were expanded for 7 days, and their genotypes were confirmed by Western blotting. Opa1-OE MEF cell line was cultured in the same manner described above, with the addition of 2.5 µg/mL puromycin in the culture media.

Human HEK 293T cells (American Type Culture Collection; ATCC) were cultured in Dulbecco's Modified Eagle Medium (DMEM) supplemented with 10% heat-inactivated FBS (HI-FBS) and 1% penicillin-streptomycin. Samples of supernatant media from cell culture experiments were analyzed monthly for the presence of mycoplasma using MycoAlert PLUS (Lonza).

To generate a HEK 293T cell line bearing an *OPA1* exon 5b knock-out, SpCas9 sgRNAs were cloned into pUC19-U6-BsmBI_cassette-SpCas9gRNA (BPK1520; Addgene ID 65777) harboring spacer sequences GCTCATTGTGAACTCGTGGCA (plasmid CJT90), GCCAACAGAAGCGCAAGGTGA (plasmid CJT91), GTTCTCCTCATTGTGAACTCG (plasmid CJT92), and GCAGAAGCGCAAGGTGATGGA (plasmid CJT93), each with added 5'Gs. Transfections were performed 20 hours following seeding of $2x10^4$ HEK 293T cells per well in 96-well plates. Transfections contained 70 ng of SpCas9 nuclease plasmid (pCMV-T7-SpCas9-P2A-EGFP (RTW3027; Addgene ID 139987) and 15 ng each of two sgRNA expression plasmids mixed with 0.3 µL of TransIT-X2 (Mirus) in a total volume of 15 µL Opti-MEM (Thermo Fisher Scientific), incubated for 15 minutes at room temperature, and distributed across the seeded HEK 293T cells. Cells were grown for approximately 72 hours prior to extracting genomic DNA (gDNA) by discarding the media, resuspending the cells in 100 µL of quick lysis buffer (20 mM Hepes pH 7.5, 100 mM KCl, 5 mM MgCl2, 5% glycerol, 25 mM DTT, 0.1% Triton X-100, and 60 ng/µL Proteinase K (New England Biolabs; NEB)), heating the lysate for 6 minutes at 65 ºC, heating at 98 ºC for 2 minutes, and then storing at -20 ºC. Editing efficiency in bulk transfected cells was assessed by next-generation sequencing (NGS) essentially as previously described (Walton *et al*, 2020) using PCR round 1 primers oLLH9-

ACACTCTTTCCCTACACGACGCTCTTCCGATCTCATCTGTTCCTTTGTTGCACCCTTGG and oLLH10-GACTGGAGTTCAGACGTGTGCTCTTCCGATCTGGAGTCCATGAACAGATTGAGGTGAC. To create cell lines, HEK 293T cells were seeded and transfected with plasmids RTW3027 and both sgRNAs CJT91 and CJT92. Transfected cells were grown for approximately 72 hours prior to dilution plating into 96-well plates and grown until confluent. Cells were transferred into 24-well plates with some cell mass reserved to extract genomic DNA (gDNA) for genotyping via PCR and NGS to verify biallelic *OPA1* exon 5b deletion between the two SpCas9-sgRNA cleavage sites.

To generate a HEK 293T cell line bearing an *OPA1* R194G mutation, SpCas9 sgRNAs were cloned into BPK1520 harboring spacer sequences GCGGCGTTTAGAGCAACAGAT (plasmid CJT87), GCGTTTAGAGCAACAGATCGT (plasmid CJT88), and GCGTTTAGAGCAACAGATCG (plasmid CJT89). Adenine base editor (ABE) plasmids included pCMV-T7-ABE8e-nSpCas9-P2A-EGFP (KAC978; Addgene ID 185910) or pCMV-T7-ABE8e-nSpG-P2A-EGFP (KAC984; Addgene ID 185911). Transfections were performed 20 hours following seeding of $2x10^4$ HEK 293T cells per well in 96-well plates and contained 70 ng of ABE8e plasmid and 30 ng of sgRNA expression plasmid mixed with 0.3 µL of TransIT-X2 (Mirus) in a total volume of 15 µL Opti-MEM (Thermo Fisher Scientific). The transfection mixtures were incubated for 15 minutes at room temperature and distributed across the seeded HEK 293T cells. Cells were grown for approximately 72 hours prior to extracting gDNA as described above. Editing efficiency in bulk transfected cells was assessed by NGS using PCR round 1 primers oLLH7-ACACTCTTTCCCTACACGACGCTCTTCCGATCTGCTTAGGCTGTTGACATCACTGGAGAATG and oLLH8-GACTGGAGTTCAGACGTGTGCTCTTCCGATCTCCAGAACTGCCACGTAATACCTTGTAC. To create cell lines, HEK 293T cells were seeded and transfected with plasmids KAC984 and CJT88. Transfected cells were grown for approximately 72 hours prior to dilution plating into 96-well plates and grown until confluent. Cells were transferred into 24-well plates with some cell mass reserved to extract genomic DNA (gDNA) for genotyping via PCR and NGS to verify biallelic introduction of *OPA1*-R194G.

Live cell epifluorescence microscopy

Confluent MEF cells were harvested, seeded onto 35 mm glass-bottom dishes (MatTek Life Sciences) coated with poly-D-lysine (0.1 mg/mL) and allowed to grow overnight at 37˚C under 5% CO_2. For visualization of mitochondria, cells were stained with 50nM MitoTracker™ Deep Red FM (Thermo Fisher Scientific) at 37˚C for 15 mins. Following three rounds of washes with 1X PBS, cells were placed in Live Cell Imaging Solution (Invitrogen). Imaging relating to figure S5 was performed using Zeiss Axio Observer Z1 Advanced Marianas™ Microscope system, an Alpha Plan-Apochromat 100x/1.46 NA Oil TIRF Objective M27 and Prime 95B scientific CMOS camera (Photometrics). MitoTracker™-stained mitochondria were imaged using “Cy5” filter set (Cy5-4040C, Excitation: 628/40 nm [608-648nm],

Emission: 692/40 nm [672-712nm], Dichroic Mirror: 660nm) (Semrock). Temperature, humidity, and CO_2 concentrations were controlled with an Okolab Microscope Stage Incubator System. Image acquisition and processing were done using SlideBook™6 (Intelligent Imaging Innovations, Inc, Denver, CO) and Fiji (Schindelin et al., 2012). Time-lapse videos of stained mitochondria were taken at one frame per 30 seconds for a duration of 5 mins.

Fluorescence imaging and quantification

To determine mitochondrial network morphology, MEF cells were seeded onto glass-bottom dishes and grown to ~80% confluency. Cells were washed with PBS and fixed in 4% paraformaldehyde (PFA) in PBS for 20 mins. Following three washes with PBS, cells were permeabilized in 0.1% Triton X-100 diluted in PBS for 5 min. Cells were incubated in 2% normal goat serum and 0.05% Triton X-100 in PBS for 1 hour, and subsequently incubated in the same buffer with 1:300 Tom20 Recombinant rabbit antibody (Invitrogen) overnight at 4˚C. After thorough washing with PBS, cells were incubated with 1:1000 goat anti-rabbit Alexa Fluor® 488 AffiniPure antibody (Jackson ImmunoResearch) for 1 hour at RT. Cells were washed in PBS and coated with UltraCruz® Aqueous Mounting Medium with DAPI (Santa Cruz) prior to imaging. Images were captured using A1R HD25 point scanning confocal with GaAsP and PMT detectors, equipped with an Apo TIRF 60x/1.49 NA objective lens and Ti2 Z-drive. Cells were manually scored into four morphological classifications (Wang et al. 2021): “Fragmented” refers to cells that contain spherical mitochondrial fragments with two or less short tubules present. “Short tubular” refers to cells containing a mixture of fragmented and short tubular mitochondria. “Long tubular” refers to cells with elongated mitochondria, but not fused into a mitochondrial mesh. “Interconnected” refers to cells with a highly interconnected network of mitochondrial filaments, with few isolated mitochondria present.

Cryo-EM specimen preparation

Cells were prepared following the deposition method. Cells were detached and counted with a hemocytometer. Quantifoil 200 mesh holey carbon R2/2 (EMS) were glow-discharged for 60s or 90s at 20mA or 15mA using a PELCO easiGlow glow discharge system (Ted Pella). ~1000-3000 cells were deposited onto a grid by pipetting 3 µL of detached cells onto the EM grid. Blotting and plunging was performed in a FEI Vitrobot Mark IV (Thermo Fisher Scientific (TFS)) at RT, 100% humidity with a waiting time of 60 seconds, one-side blotting time of 15 seconds and blotting force of 10 or 7. Customized parafilm sheets were used for one-sided blotting. All subsequent grid handling and transfers were performed in liquid nitrogen. Grids were clipped onto cryo-FIB autogrids (TFS).

Cryo-FIB milling

Grids were loaded in an Aquilos 2 Cryo-FIB (TFS). Specimen was sputter coated inside the cryo-FIB chamber with inorganic platinum, an integrated gas injection system (GIS) was used to deposit an organometallic platinum layer to protect the specimen surface and avoid uneven thinning of cells (Wagner *et al*, 2020). Cryo-FIB milling was performed on the specimen using two rectangular patterns to mill top and bottom parts of cells, and two extra rectangular patterns were used to create macro-expansion joints to improve lamellae instability (Wolff *et al*, 2019). Cryo-FIB was performed at a nominal tilt angle of 14-26 which translates into a milling angle of 7-19. Cryo-FIB milling was performed in several steps of decreasing ion beam current ranging from 1 nA to 10 pA and decreasing thickness to obtain 200-400 nm lamellae.

Cryo-electron tomography

All imaging was performed on a FEI Titan Krios (TFS) transmission electron microscope operated at 300KeV equipped with a Gatan BioQuantum K3 energy filter (20eV zero-loss filtering and a Gatan K3 direct electron detector. Prior acquisition, a full K3 gain reference was acquired, and ZLP and BioQuantum energy filter were finely tuned. The nominal magnification for data collection was 33,000x giving a calibrated 4K pixel size of 2.758. Data collection was performed in nanoprobe mode using SerialEM (Mastronarde, 2003) or TFS Tomography 6 software. The tilt range varied depending on the lamella, but generally was from -70 to 70 in 2 steps following the dose-symmetric scheme (Hagen *et al*, 2017). Tilt images were acquired as 8K x 11K super-resolution movies of 6 frames with a set dose rate of 1.5-3 e-/Å/sec. Tilt series were collected at a range of nominal defoci between -3.5 and -5 µm and a target total dose of 100 to 180 e-/Å (Supplementary Table 1).

Cryo-electron tomography image processing

Acquired tilted super-resolution movies were motion corrected and Fourier cropped to 4K x 5K stacks, minimizing aliasing effects using *framealign* from IMOD (Kremer *et al*, 1996). Tilt-series were aligned using etomo in IMOD (Mastronarde & Held, 2017). CTF-estimation was performed in IMOD (Turoňová *et al*, 2017) and/or using customized MATLAB scripts. CTF-correction was performed by *ctfphaseflip* program in IMOD. CTF-corrected unbinned tomograms were reconstructed by weighted back projection with and without a SIRT-like filter and subsequently 2x, 4x and 8x in IMOD. Cryo-electron tomograms were denoised using Topaz (Bepler *et al*, 2020) and summed projection of cryo-tomogram slices were performed in *Dynamo* (Castaño-Díez *et al*, 2012) complemented with customized MATLAB scripts.

3D Segmentation

Segmentation was done in TomoSegMemTV (Martinez-Sanchez *et al*, 2014) to create the first triangulation of mitochondrial membranes. Such triangulation was refined using Amira (TFS) by unbiased semi-automatic approaches. Final triangulated surfaces were remeshed and smooth in Amira for final rendering.

Quantitative analysis of cryo-ET data

Mitochondrial shape

Mitochondria morphology was categorized into 'ellipsoidal', 'round', 'heart-shaped' (when displaying a polygon shape) and 'partial' (when mitochondria was out of the XY image) by visual inspection of cryo-electron tomograms.

Mitochondrial size

Mitochondria were outlined in summed projection images of the central slices of cryo-electron tomograms in FIJI using the 'polygon selection' tool and pressing the measure key to output the area of outline mitochondria in nm^2.

Mitochondrial coverage

Mitochondrial area in μm^2 obtained from mitochondria size measurements was divided by the total area of the summed projected image.

Matrix density: Mitochondria density was measured in summed projection images of the central slices of cryo-electron tomograms that were all equally grey scale normalized in FIJI by applying the function equalize histogram set at 0.35% for all images. Three lines were drawn in the matrix region of the mitochondria under analysis and their mean grey value was calculated by pressing the measure button in FIJI (Schindelin *et al*, 2012). Three measurements per mitochondria were obtained, thus, the mean was calculated to obtain a single value per mitochondrial matrix.

Cristae density

Number of cristae was quantified in cryo-electron tomogram using the multi-point tool in FIJI. The number of cristae was normalized against area of mitochondria in μm^2.

Mitochondrial volume: Total mitochondria volume was calculated in Amira by summing the volume of cristae lumen (CL), inter membrane spacing (IMS) and matrix volume in μm^3. CL, IMS and matrix volumes was outputted by Amira based on the 3D surface of each compartment segmented and rendered in Amira with the module 'measure surface'. Ratios were calculated by dividing the volume values of the specified mitochondrial compartments.

Cristae directionality

Cristae was classified as 'straight', 'tilted' or 'disconnected' by visual inspection of cryo-electron tomograms.

Cristae shape

Cristae was classified as 'lamellar', 'globular', 'tubular' or 'unusual' by visual inspection of cryo-electron tomograms. Within the category 'unusual' the following classes were defined: 'loop' when cristae present two cristae connection with the IMS and was curved, 'pinching' when cristae membranes presenting punctual touching points, 'straight-across' when cristae present two cristae connection with the IMS just opposite to each other forming a straight septum-like structure across a mitochondrion, 'amorphous' when cristae displayed an irregular polygon shape, 'splitting' when cristae branched into two or more cristae within a giving mitochondrion, 'ring' when cristae formed a circular ring within mitochondria, 'zip' when cristae membranes come close and only one membrane was distinguished that later opens up into regular lamellar cristae, and 'vesicular' when cristae was wide, usually amorphous, but contained electron dense material resembling to membranes.

Cristae length

Cristae length was measured in cryo-electron tomograms by extracting the cristae volumes in *Dynamo* using the 'oblique slices in tomoslice' tool (https://wiki.dynamo.biozentrum.unibas.ch/w/index.php/Oblique_slices_in_tomoslice). Then, length was computing using the length tool in *Dynamo* (https://wiki.dynamo.biozentrum.unibas.ch/w/index.php/Walkthrough_on_GUI_based_tilt_series_alignment_(EMBO2021)#Visualization_matrix).

Cristae width

Subtomogram averaging was performed in *Dynamo*. Particles were manually identified using '*dtmslice*' interface in *Dynamo* (Navarro *et al*, 2018, 2020). Subtomograms with a size of $(1058.8)^3$ Å were extracted from 4x-binned tomograms. An initial reference generated from a random set of particles was used for 3D particle alignment. A total of 12 iterations were used to align particles until convergence, i.e., until no further improvement of alignment parameters was detected by additional iterations, and then final averages were obtained. Final averages were generated from 222 (WT), 430 (OE-Opa1), 323 l-Opa1*, 653 s-Opa1* and 243 KO-Opa1 subtomograms. EM densities were visualized in UCSF Chimera (Pettersen *et al*, 2004). Cristae width is measured per particle in 3D width measurement was done in *Dynamo* by cross-correlation of each particle against a set of 40 templates displaying a distance range between membranes of 1 to 40 pixels (corresponding to 2.2 to 88 nm distance, https://wiki.dynamo.biozentrum.unibas.ch/w/index.php/Framework_for_estimation_of_membrane_thickness_and https://github.com/NavarroPP/membraneThickness/blob/main/CristaeThickness.m). A cross-correlation peak per particle is outputted corresponding to the distance value between the two cristae membranes defined here as cristae width (Fig. S7).

Cristae junction measurement

Cristae junctions were measured in summed projection images of 10 slices from each tomogram. Each CJ was isolated, and the width was measured using the line tool and measurement function in FIJI (Schindelin *et al*, 2012). The angle of each CJ was measured using the angle tool and measure function in FIJI. If a CJ was visible in multiple and nonoverlapping sections of the tomograms, multiple measurements were made for that CJ and averaged to represent the overall 3D shape of the CJ.

Statistical analysis

Statistical tests performed to assess differences in our quantifications were chosen based on the distribution of the data points. Since most of our data did not follow a normal distribution, we used non-parametric tests as Mann-Whitney test in order to measure significant difference between two data sets (e.g., WT vs Opa1-OE). When both data sets followed normal distribution unpaired t test with Welch's correction was used since standard deviations were different between the compared data sets. Furthermore, additional statistical tests were applied to reassure statistical results outputting very similar p values and same significance. All statistical analyses were performed in Prism 9 GraphPad software.

Mitochondrial respiration assays

Cells were seeded in a Seahorse XFe96 Cell Culture plate in 80µL of DMEM supplemented with 10% FBS and 1% penicillin/streptomycin at a concentration of 30,000 cells/well and left to recover at 37°C in 5% CO_2 for 6 hours. After, cells were then washed three times with prewarmed assay buffer (XF Seahorse DMEM media supplemented with 10mM Seahorse XF Glucose, 1mM Seahorse XF Pyruvate, and 2mM Seahorse XF L-Glutamine), covered with 180µL of assay buffer, and incubated for one hour at 37°C under no atmospheric CO_2. Prior to the assay, the injection ports on the sensor cartridge were loaded with 2.0µM oligomycin, 1µM carbonyl cyanide-*p*-trifluoromethoxyphenylhydrazone (FCCP), and 0.5µM of rotenone/antimycin A. Before the injection of drugs, the Seahorse XFe96 Analyzer mixed the assay media for each well for 10 minutes and took three baseline measurements. After the injection of each drug, the analyzer mixed for 3 mins, waited for 1 min, and the measured for 3 mins, three times. Oxygen consumption rates (OCRs) are the average oxygen consumption rate during each three-minute measurement time and were normalized to cells/well. Biological replicates indicate assay performed on different flasks of MEF cell culture grown under the same condition and passage number. Statistical analysis performed to assess differences in our measurements were chosen based on the distribution of the data points. The mitochondrial respiration data followed a normal distribution by the Shapiro-Wilk normalcy test. We used unpaired t test with Welch's correction to evaluate significance as standard deviations were different between the compared data sets. All statistical analyses were performed in Prism 9 GraphPad software.

BH3 profiling and chemosensitivity methods

BH3 profiling was conducted by flow cytometry according to published protocols (Fraser *et al*, 2018). Briefly, cells in culture were trypsinized and added to wells of prepared 96 well plates containing the indicated peptide conditions and .001% digitonin in mannitol experimental buffer (MEB; 10 mM HEPES (pH 7.5), 150 mM mannitol, 50 mM KCl, 0.02 mM EGTA, 0.02 mM EDTA, 0.1% BSA, and 5 mM succinate). Peptide treatments were carried out for 60 minutes at 28 degrees C, then cells were fixed for 10 minutes in 2% PFA. Fixation was quenched with N2 buffer (1.7 M tris base and 1.25 M glycine (pH 9.1)), then cells were stained overnight with DAPI and an Alexa Fluor 647-conjugated anti-cytochrome c antibody (Biolegend, clone 6H2.B4). Stained cells were analyzed using an Attune NxT flow cytometer, with gates drawn based on cytochrome c staining in the negative and positive control treatments (PUMA2A and DFNA5 peptide). The percentage of cytochrome c negative cells was reported for each peptide treatment condition**.**

For chemosensitivity assays, cells were plated at 10^4 cells per well in 100 µl culture medium on 96-well flat-bottom plates (Denville). They were treated with the following drugs at specified concentrations: etoposide 10 µM, staurosporine 0.1 µM, and doxorubicin 1 µM. After 24 hours in standard tissue culture conditions, cells were stained with Alexa Fluor 488-conjugated Annexin V in 10× Annexin binding buffer [0.1 M Hepes (pH 7.4), 1.4 M NaCl, and 25 mM $CaCl_2$ solution]. Alexa Fluor 488-conjugated Annexin V was added to the solution at a 1:500 dilution. The staining solution was added to the cells at a 1:10 dilution, and the cells were allowed to stain for 20 minutes on ice in the dark. Annexin V positivity was measured by Attune flow cytometer equipped with an autosampler (Thermo Fisher Scientific). Biological replicates indicate assay performed on different flasks of MEF cell culture grown under the same condition and passage number. Statistical analysis was performed using a two-way ANOVA with Holm-Sidak's correction for multiple hypothesis since the data were normally distributed (Fraser *et al*, 2022; Singh *et al*, 2023). All statistical analyses were performed in Prism 9 GraphPad software.

Mitochondrial Calcium Retention Capacity (CRC) Assays

MEF cells (1 x 10^6) were incubated in 150 µl assay buffer (125 mM KCl, 20 mM HEPES, 2 mM K_2HPO_4, 5 mM glutamate, 5 mM malate, 5 mM succinate, 1 mM $MgCl_2$, 5 µM EGTA, 1 µM Calcium Green 5N, 40 µM digitonin, pH 7.2) supplemented with 1.5 µM thapsigargin (Sigma) for 10 mins. Fluorescence was continuously monitored using a PerkinElmer EnVision plate reader (excitation, 485 nm; emission, 535 nm). Sequential 30 µM $CaCl_2$ pulses were administered until Ca^{2+} uptake ceased, and a sudden release of previously taken up Ca^{2+} indicated by a sustained increase in fluorescence reading, consistent with mPTP opening. Biological replicates indicate assay performed on different flasks of MEF cell culture grown under the same condition and passage number.

Mitochondrial network and mtDNA imaging and analysis by instant Structured Illumination Microscopy (iSIM)

For live-cell imaging, cells were stained with PKMito Orange probe (Spirochrome) and SYBR™ Gold Nucleic Acid Stain (Thermo Fisher Scientific), following manufacturer's instructions. 250 nM PKMito Orange and 1:10 000 SYBR™ Gold Nucleic Acid Stain were the optimal concentrations for the cell type. Cells were allowed to rest for 1-2 hours before imaging. Instant structured illumination microscopy (iSIM) was performed on the custom-built microscope set-up at the EPFL Laboratory of Experimental Biophysics (York *et al*, 2013; Mahecic *et al*, 2020). Time-lapse images were acquired from MEF cells acclimatized in a 37 °C chamber, using 488-nm and 561-nm excitation lasers, a 1.49 NA oil immersion objective (APONXOTIRF; Olympus), and an sCMOS camera (PrimeBSI, 01-PRIME-BSI-R-M-16-C; Photometric), with additional fast vertically scanning piezo actuated mirrors for scanning/illumination pattern homogenization. The raw images were deconvolved using the Richardson Lucy algorithm as implemented by the flowdec Python package (Czech *et al*, 2019) with 10 iterations. Deconvolved iSIM images of stained MEF cells were processed and analyzed using the CellProfiler™ software (Stirling *et al*, 2021). Briefly, mitochondria were segmented from the PKMito Orange signal using the Robust Background thresholding algorithm with 2 standard deviations following median filtering, which was subsequently used to mask and segment the nucleoid foci from the SYBR™ Gold image (Gaussian filtering and Robust Background algorithm with 2 standard deviations). The size and shape of each segmented object were then measured, and each cell's values are displayed normalized to the segmented mitochondrial area. These data are not normally distributed, thus we used Mann-Whitney test to measure significant difference between WT and the other cell lines. All statistical analyses were performed in Prism 9 GraphPad software.

Quantification of mtDNA by qPCR

Total genomic DNA was extracted using Qiagen DNeasy kit following manufacturer's protocol and 30 ng DNA was used for each qPCR reaction. Two mitochondrial probes were each normalized to a nuclear probe to calculate mtDNA copy number relative to nuclear genome copies. This relative mtDNA copy number for all genotypes were then normalized to that of WT MEF. Biological replicates indicate assay performed on MEF cell culture derived from different flasks, grown under the same condition and passage number. Sequences of qPCR primers:

MT-16S Fwd: CCGCAAGGGAAAGATGAAAGAC

MT-16S Rev: TCGTTTGGTTTCGGGGTTTC

MT-ND1 Fwd: CTAGCAGAAACAAACCGGGC

MT-ND1 Rev: CCGGCTGCGTATTCTACGTT

nuclear HK2 Fwd: GCCAGCCTCTCCTGATTTTAGTGT

nuclear HK2 Rev: GGGAACACAAAAGACCTCTTCTGG

These data followed a normal distribution by the Shapiro-Wilk normalcy test. We used unpaired t test with Welch's correction to evaluate significance as standard deviations were different between the compared data sets. All statistical analyses were performed in Prism 9 GraphPad software.

941

942 **Figure 1 | *In situ* mitochondrial membrane morphology is influenced by Opa1 processing.**
943 Mitochondria with distinguishable inner mitochondrial membrane (IMM) and outer mitochondrial
944 membrane (OMM) visualized by cryo-ET. **(a)** (Right) Summed, projected central slices of cryo-electron
945 tomograms visualizing representative mitochondria in indicated MEF cell lines. (Left) Three-dimensional
946 (3D) rendering of segmented membranes with mitochondria shown across Z slices. Green and yellow
947 surfaces indicate OMM and IMM, respectively. (Bottom right) Schematic of Opa1 forms present in
948 respective cell lines. **(b)** Graph bar representing the relative proportion of different mitochondrial shapes
949 observed. **(c)** Plot of mitochondria size (μm^2) observed in cryo-electron tomograms in MEF lines. Scatter
950 plots show data distribution, the mean is marked by a bold black line. Significance of difference is tested
951 relative to wild type using Mann Whitney test; *p<0.05, **p<0.01, ****p< 0.0001. N refers to number of
952 mitochondria: wild-type = 57, Opa1-OE = 17, l-Opa1* = 39, s-Opa1* = 55, Opa1-KO = 12. Scale bar =
953 200 nm.
954
955 **Fig. 2 | *In situ* crista ultrastructure. (a)** Graph bars showing the proportions of straight, tilted, and no
956 attachment observed (NAO) crista and **(b)** of lamellar, tubular, globular and unusual crista observed in
957 indicated MEF lines. **(c)** Measured cristae length and **(d)** cristae width across cell lines. **(e)** (Top rows)
958 Computational slices of straight, tilted, disconnected, globular and tubular crista across cell lines and the
959 corresponding 3D renderings (bottom rows) from cryo-electron tomograms (n.a. =not applicable). **(f)**
960 Histograms of crista widths across cell conditions (see Methods). **(g)** Subtomogram averages of
961 mitochondrial cristae membranes with the average width indicated. Scatter plots show data distribution,
962 the mean is marked by a bold black line. Removal of outliers did not change statistical test results (see
963 source data). Significance of difference is tested relative to WT using Mann Whitney test; *p<0.05,
964 ***p<0.001, ****p<0.0001. For (a) and (b): N refers to the number of cristae analyzed: wild-type = 131,
965 Opa1-OE = 166, l-Opa1* = 380, s-Opa1* = 495, Opa1-KO = 112. For (c): N = 50 for all cell lines. For (d)
966 and (f): N refers to the number of cristae subvolumes: WT = 222, Opa1-OE = 430, l-Opa1* = 323, s-
967 Opa1* = 653, Opa1-KO = 243. For (d) mean ± SD in WT = 14.5±5.8; Opa1-OE = 15.2±10.5; l-Opa1* =
968 17.6±15.4; s-Opa1* = 12.9±7.9; Opa1-KO = 20±15.8. Scale bar = 50 nm.
969
970 **Fig. 3 | Quantification of cristae junction (CJ) properties. (a)** Plots of measured cristae junction width
971 and **(b)** angle across cell lines (see Fig. S8c, d and Methods section for measurement methods). **(c)**
972 (Top) Summed, projected central slices of cryo-electron tomograms of representative mitochondria
973 analyzed in (a) and (b) with magnified cristae junction (bottom insets). Scatter plots show data distribution,
974 the mean is marked by a bold black line. Significance of difference is tested relative to wild type using

Mann Whitney test; *p<0.05, **p<0.01, ***p<0.001. N refers to number of cristae analyzed: wild-type = 103, Opa1-OE = 33, l-Opa1* = 107, s-Opa1* = 92, Opa1-KO = 34. Scale bar = 100 nm. Inset scale bar = 25 nm.

Fig. 4 | l-Opa1* cells show WT apoptotic priming. (a) BH3 profiling of MEF lines with BIM BH3 peptide at indicated concentrations compared with positive control DFNA5 and negative control PUMA2A. N = 3-4 biological replicates (see methods for description). Significance of difference is tested relative to wild-type using the Holm-Sidak's multiple comparison test; *p<0.05, **p<0.01, ***p<0.001, ****p<0.001. **(b)** MEF lines were treated with indicated agents for 24h and apoptosis was detected via flow cytometry after staining with Annexin V. N = minimum 4 biological replicates. **(c)** Representative traces of mitochondrial calcium retention capacity assays done in indicated MEF lines. **(d)** Quantification of $CaCl_2$ concentration required to induce mPTP opening in (c). N = 3 biological replicates.

Fig. 5 | Defects to mitochondrial functions are observed in cells with altered Opa1 levels. (a) OCR plotted against time with the addition of each compound indicated by an arrow for oligomycin (2µM), FCCP (1 µM), and rotenone/antimycin A (0.5µM). **(b)** Aspects of mitochondrial respiration; basal respiration rates, the amount of respiration used for ATP production, maximum respiration and spare capacity, are extracted by the data plotted in (a). N = 3 biological replicates. Significance of difference is tested relative to WT using Welch's t-test; *p<0.05, **p<0.01, ***p<0.001.

Fig. 6 | Summary of cryo-ET cristae observations. Cartoon schematic summarizing mitochondrial morphological observations dependent on Opa1 state. Mitochondria in l-Opa1* cells displayed WT-like CJ widths and perpendicularity. The majority of mitochondria displayed a stacking phenotype and multi-junction cristae. Tubular and vesicular cristae were found in s-Opa1* cells. Summaries of functional dysfunctions corresponding to observed cristae morphological changes. (a) Respiratory defects correlate with a large number of unstructured cristae. (b) Defects in cytochrome c (CytC) release properties (as evaluated by BH3 profiling) and calcium handling correlate with wider CJ and vesicular cristae. Cartoon schemes with hypothesized modes of action for l-Opa1 in the (c) crista stacking, and (d) BH3 and calcium handling process.

Supplementary Figure S1 | Presence of Opa1 forms per MEF cell line. (a) (Top) Western blot detection of Opa1 forms in indicated MEF cell lines using Opa1 antibody. (Bottom) Actin was used as loading control. **(c)** Genetic schematic and cartoon depictions of Opa1 forms present in MEF cell lines used in this study.

Supplementary Figure S2 | Gallery of cryo-ET data. (a) Summed, projected central slices of cryo-electron tomograms visualizing mitochondria in wild-type, Opa1-OE, l-Opa1*, s-Opa1* and Opa1-KO MEF. White arrowheads indicate calcium deposits, blue arrowheads indicate ellipsoidal mitochondria and purple arrowheads indicate round mitochondria. **(b)** Mitochondria size (μm^2) broken down by shape per cell line. Scatter plots show data distribution, the mean is shown by a bold black line. Significance of difference is tested relative to wild type using Mann Whitney; ****p<0.0001. For b: N refers to number of mitochondria: wild-type = 57, Opa1-OE = 17, l-Opa1* = 39, s-Opa1* = 55, Opa1-KO = 12. Scale bar = 200 nm.

Supplementary Figure S3 | Mitochondrial subcompartment volumes. (a) Three-dimensional renderings of segmented inter-membrane space (IMS, pink surface), cristae lumen (CL, magenta surface), and matrix (translucent grey surface) volumes. **(b)** Total mitochondrial volume across indicated cell lines. **(c)** Quantification of IMS volume, **(d)** CL volume and **(e)** matrix volume relative to total volume of each mitochondrion indicated in (b). **(f)** CL to matrix ratio and **(g)** normalized grey scale mitochondrial matrix value across cell lines. (**h**) Graph bar representing percentage of cells with detected calcium deposits in cryo-electron tomograms. Scatter plots show data distribution, the mean is shown by a bold black line. Significance of difference is tested relative to wild type using Mann Whitney test in b, d, e, g; *p<0.05, **p<0.01, ***p<0.001, ****p<0.0001; and unpaired t test in (c): **p<0.01; N refers to number of cells, for b-g: N = 5 for all cell lines. For h: N refers to the number of mitochondria: wild-type = 57, Opa1-OE = 17, l-Opa1* = 39, s-Opa1* = 55, Opa1-KO =12. Scale bar = 200 nm.

Supplementary Figure S4 | Cristae analysis. (a) Cristae density (cristae per μm^2) and **(b)** Number of cristae per mitochondria represented as scatter plots. **(c)** (Top) Summed, projected central slices of cryo-electron tomograms visualizing mitochondria with stacking crista characteristics, supported by 3D representations consisting of their sub compartments (bottom) in indicated MEF lines. **(d)** Graph bar representing percentage of mitochondria with stacking crista formation in each MEF line. For a: N refers to number of cells, N: wild-type = 33, Opa1-OE = 7, l-Opa1* = 21, s-Opa1* = 28, Opa1-KO = 11. For b:

N wild-type = 51, Opa1-OE = 17, l-Opa1* = 39, s-Opa1* = 55, Opa1-KO = 12. For (c) and (d): N wild-type = 57, Opa1-OE = 17, l-Opa1* = 39, s-Opa1* = 55, Opa1-KO = 12. Scale bar = 200 nm.

Supplementary Figure S5 | Mitochondrial network morphology in MEF lines by fluorescence microscopy. Representative images of mitochondrial morphology in indicated MEF lines labeled with MitoTracker™ Deep Red FM. Insets show magnified view of regions indicated with dashed boxes. Scale bar = 10 µm. Inset scale bar = 5 µm. (**b**) Graph bar representing mitochondrial network morphology scored in indicated MEF lines. N = 100 cells analyzed per cell line.

Supplementary Figure S6 | Unusual cristae morphology. (a) Graph bar representing the relative proportion of unusual cristae morphology observed in indicated MEF lines. Unusual cristae were categorized into vesicular, zipped, ring, split, amorphous, straight-across, pinched and loop. N refers to number of cristae analyzed, N: wild-type = 222, Opa1-OE = 430, l-Opa1* = 323, s-Opa1* = 653, Opa1-KO = 243. **(b)** Summed, projected central slices of cryo-electron tomograms showing examples of unusual cristae in mitochondria across cell lines in 2D (top) and 3D (bottom). Loop, ring, straight-across, pinched, vesicular, and amorphous cristae are shown. Scale bar = 200 nm.

Supplementary Figure S7 | Cristae length, width quantification, junction width, angle. **(a)** Cartoon schematics representing sub-tomogram averaging (STA) approach for measuring crista length and **(b)** width in 3D. **(c)** Cartoon schematic for measurement of cristae junction width and **(d)** angle. See Methods for details.

Supplementary Figure S8 | **Multijunction cristae. (a)** Scatter plot showing the percentage of multijunction cristae per mitochondrion in indicated MEF lines. **(b)** Graph bar representing percentage of multijunction cristae categorized into straight-across and loop morphology in each MEF line. Scatter plot shows data distribution, the mean is marked by a bold black line. Significance of difference is tested relative to wild type using Mann Whitney; ****p<0.0001. N refers to number of cristae, for (a), N: WT = 18, Opa1-OE =5, l-Opa1* = 30, s-Opa1* = 16, Opa1-KO = 3. For (b), N: WT = 26, Opa1-OE = 9, l-Opa1* = 79, s-Opa1* = 29, Opa1-KO = 4.

Supplementary Figure S9 | **Cell viability following apoptotic priming.** Assessment of cell viability by Annexin V staining in MEF cell lines after treatment with the indicated compounds for **(a)** 48 hours and **(b)** 72 hours. N = minimum 4 biological replicates.

Supplementary Figure S10 | **Oma1$^{-/-}$ cell functional characterization. (a)** BH3 profiling of WT and Oma1$^{-/-}$ MEF for sensitizer BIM BH3 and PUMA. N = 3 biological replicates. **(b)** Representative traces of mitochondrial calcium retention capacity assays done in indicated MEF lines. **(c)** OCR plotted against time for indicated MEF lines. **(d)** Aspects of mitochondrial respiration; basal respiration rates, the amount of respiration used for ATP production, maximum respiration, and spare capacity, are extracted by the data plotted in (c). N = 3 biological replicates. Significance of difference between l-Opa1* and Oma1$^{-/-}$ is tested using Welch's t-test; *p<0.05, **p<0.01, ***p<0.001.

Supplementary Figure S11 | mtDNA maintenance characterization. (a) Representative live iSIM images of mitochondrial network (PKmito Orange, in green) and nucleoid signal, (SYBR Gold, in magenta). **(b)** Quantification of mean nucleoid area and **(c)** total nucleoid number per cell, normalized to mitochondrial area and relative to the experimental controls (median of WT cells imaged on the same day). Significance of difference is tested relative to wild type using Mann Whitney; *p<0.05, **p<0.01, ***p<0.001, ****p<0.0001. N refers to the number of quantified cells per MEF line, WT = 83, Opa1-OE =51, l-Opa1* = 31, s-Opa1* = 55, Opa1-KO = 58. **(d)** qPCR-based determination of mtDNA (RNR2 and ND1 probes) copy number relative to nuclear genome copies (HK2 probe), normalized to WT cells. Significance of difference is tested relative to wild type using Welch's t-test; **p<0.001. N refers to 3 biological replicates. Scale bar = 10 µm.

Movie 1: 3D renderings of WT mitochondrial membranes (OMM in green and IMM in yellow) and subcompartments (IMS in pink and CL in magenta) on tomogram Z slices in XY orientation. Scale bar = 200 nm.

Movie 2: 3D renderings of Opa1-OE mitochondrial membranes (OMM in green and IMM in yellow) and subcompartments (IMS in pink and CL in magenta) on tomogram Z slices in XY orientation. Scale bar = 200 nm.

Movie 3: 3D renderings of l-Opa1* mitochondrial membranes (OMM in green and IMM in yellow) and subcompartments (IMS in pink and CL in magenta) on tomogram Z slices in XY orientation. Scale bar = 200 nm.

Movie 4: 3D renderings of s-Opa1* mitochondrial membranes (OMM in green and IMM in yellow) and subcompartments (IMS in pink and CL in magenta) on tomogram Z slices in XY orientation. Scale bar = 200 nm.

Movie 5: 3D renderings of Opa1-KO mitochondrial membranes (OMM in green and IMM in yellow) and subcompartments (IMS in pink and CL in magenta) on tomogram Z slices in XY orientation. Scale bar = 200 nm.

Movie 6: Live-cell fluorescence microscopy of MitoTracker™ Deep Red FM-stained mitochondria in indicated MEF cell lines. Movies were taken at 30 seconds per frame for 5 mins. Playback at 2 frames per second (60x real-time). Scale bar = 10 µm.

a

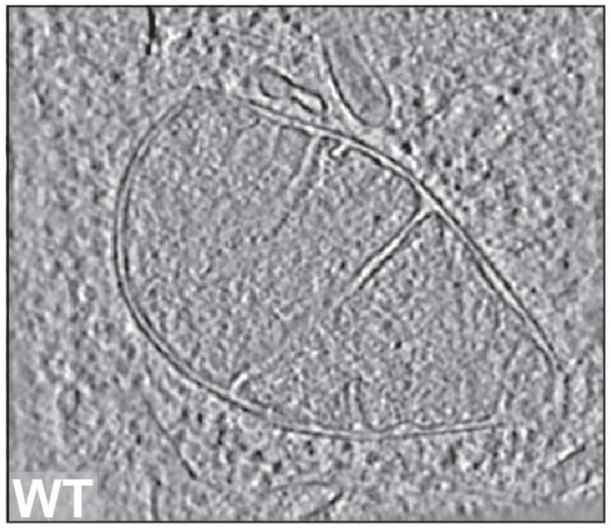

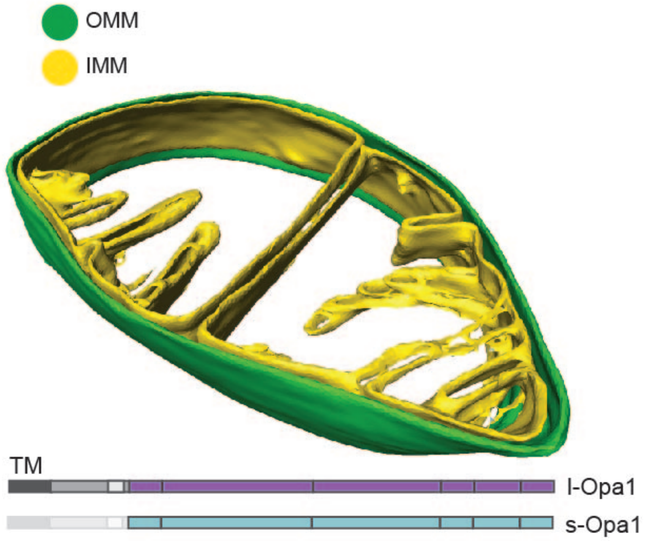

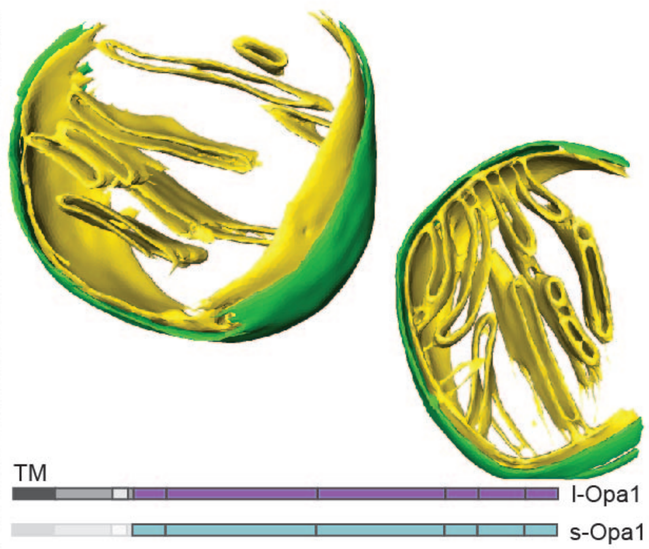

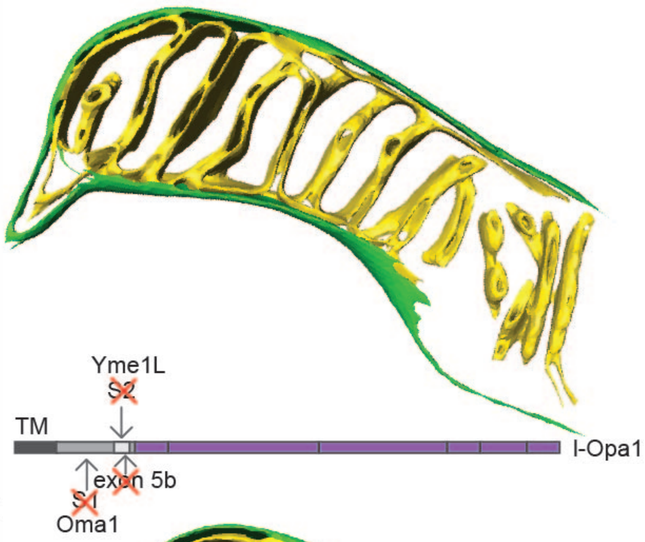

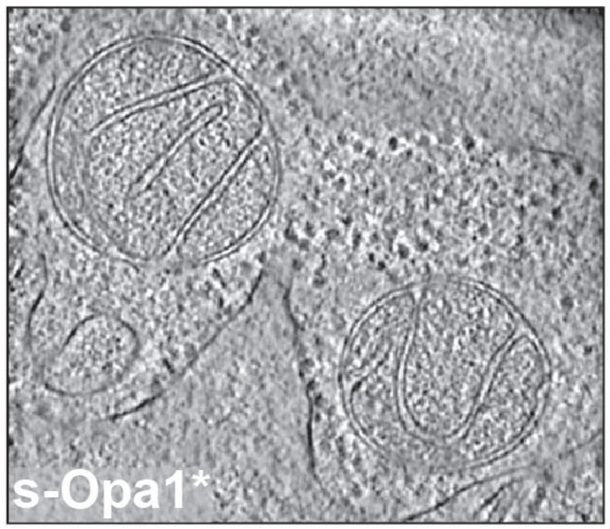

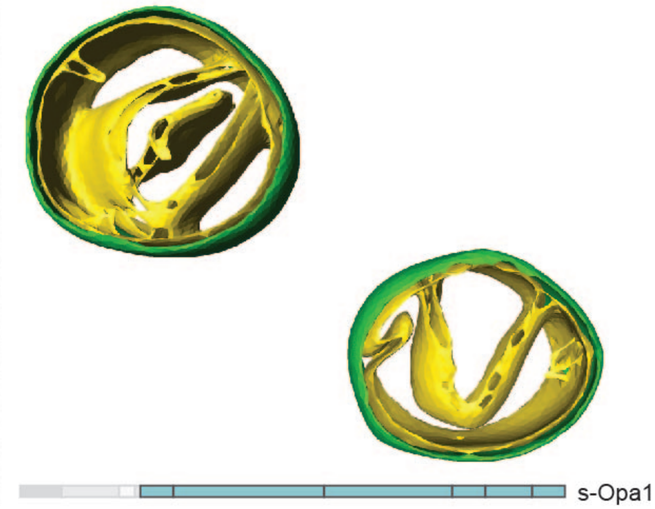

b

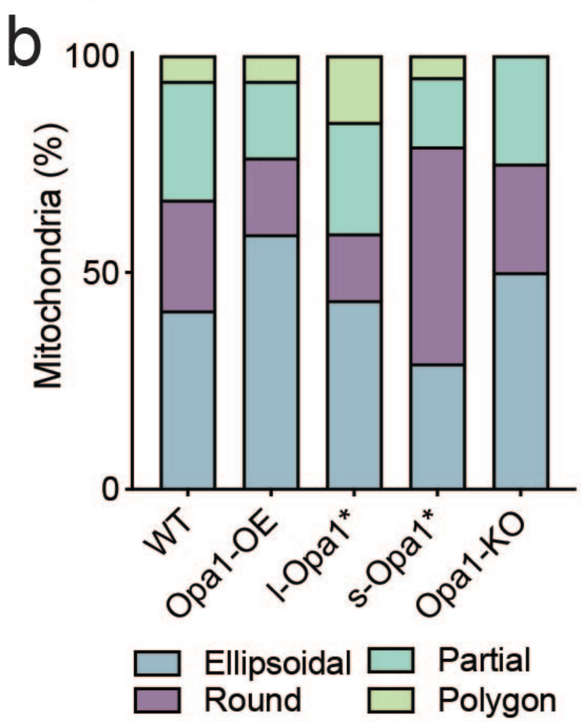

c

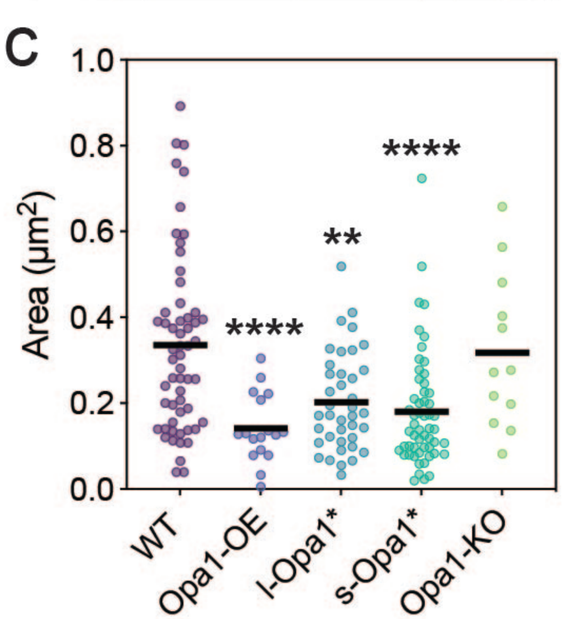

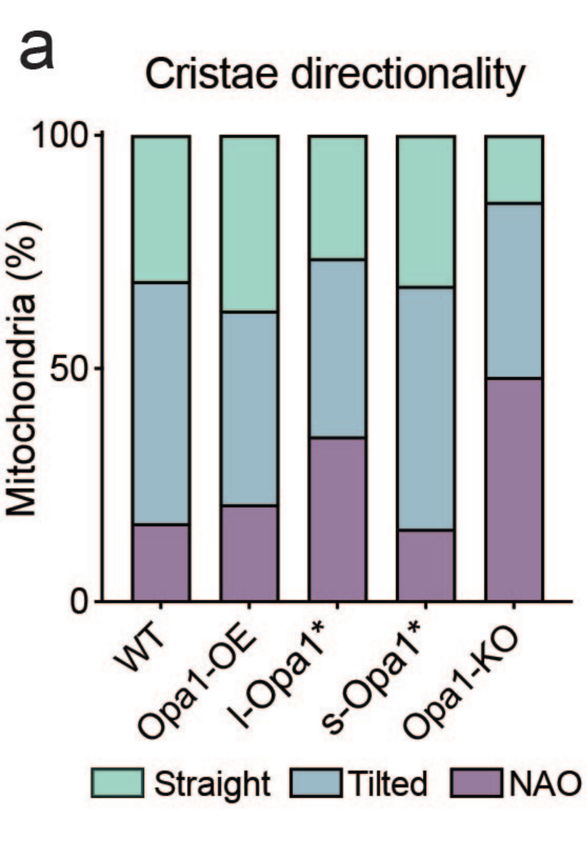

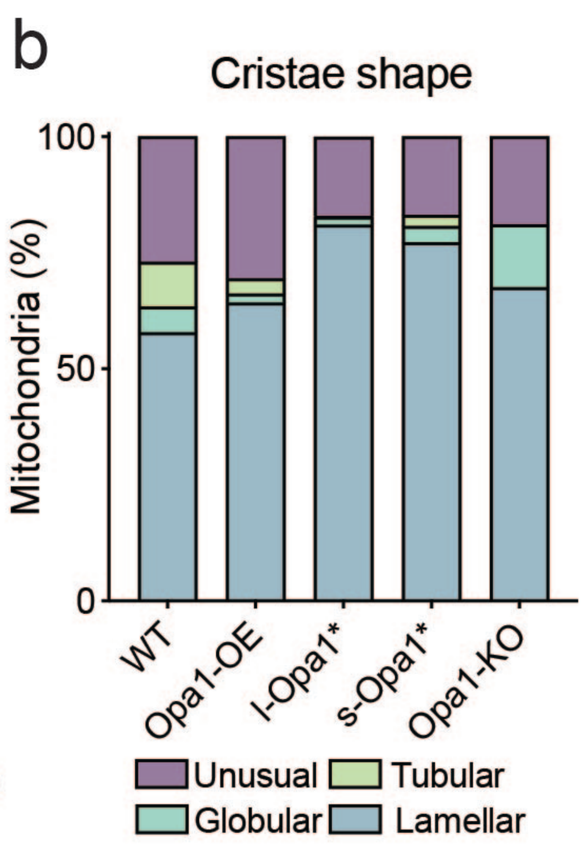

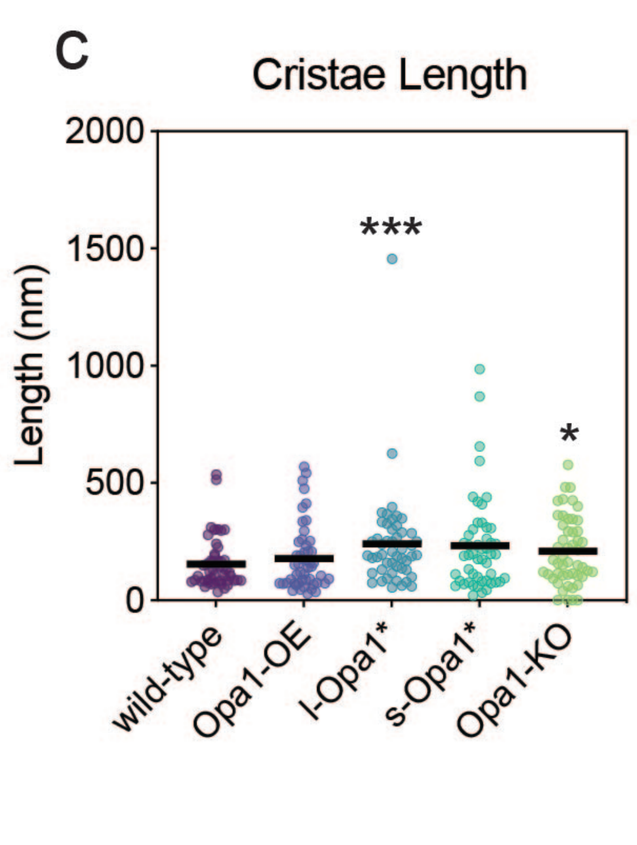

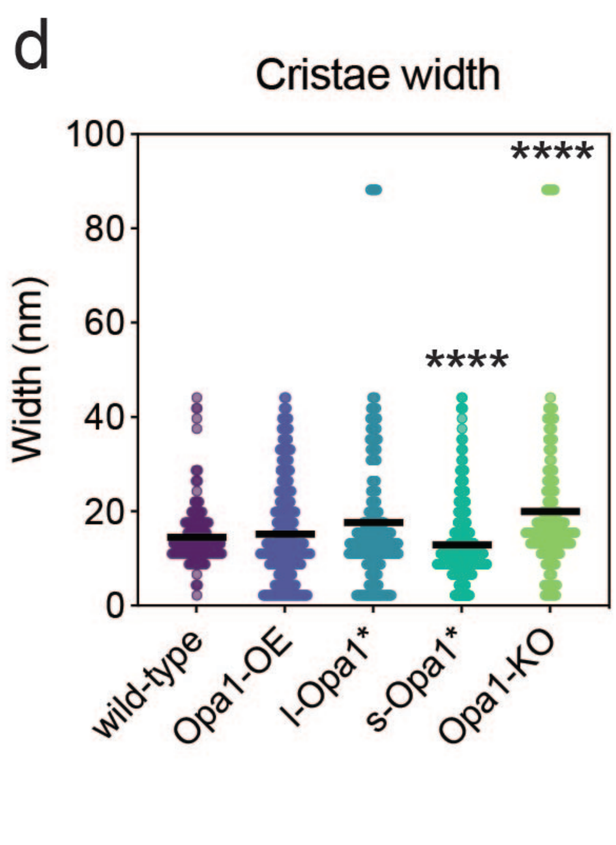

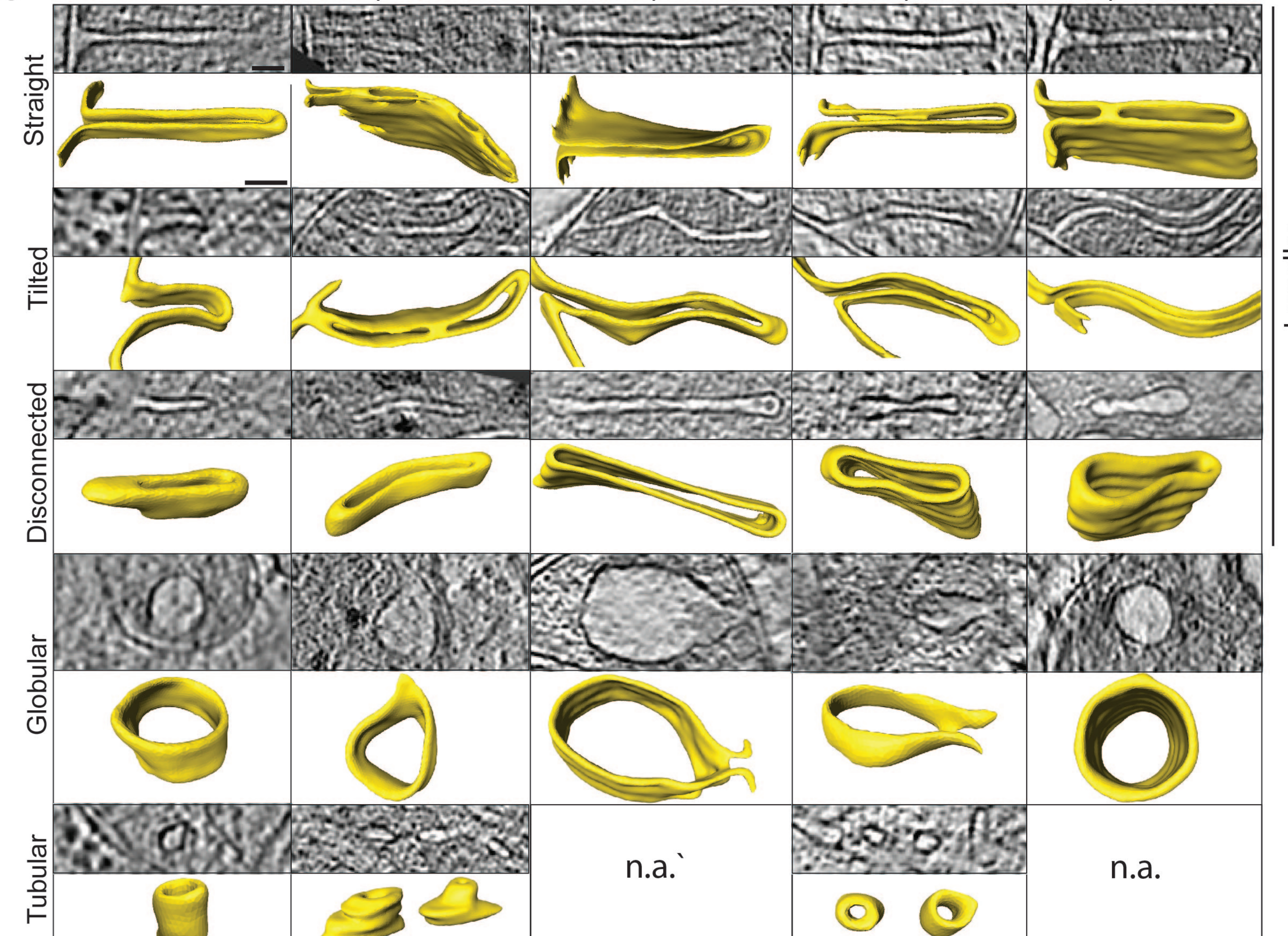

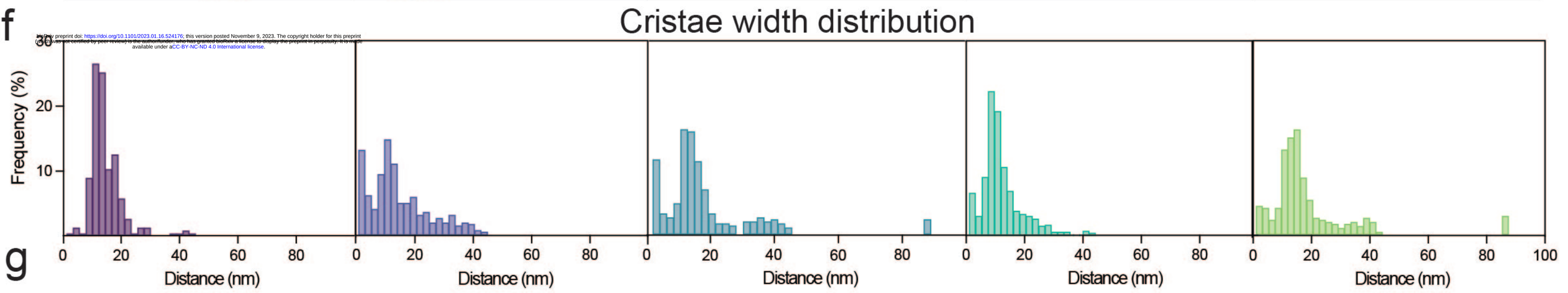

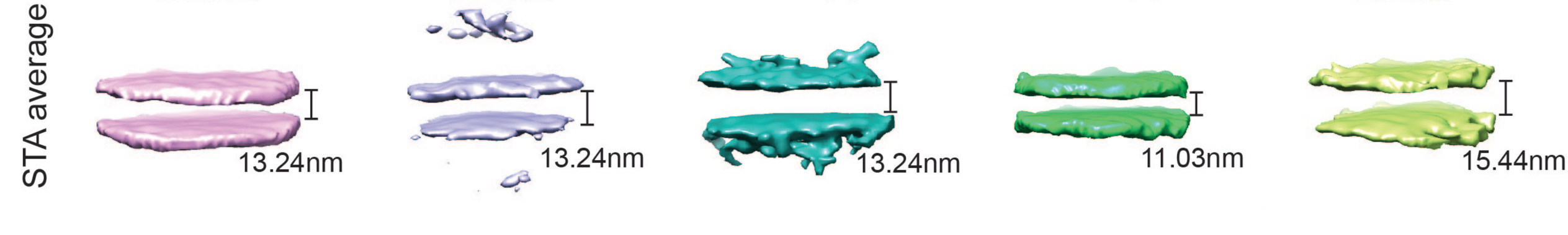

a

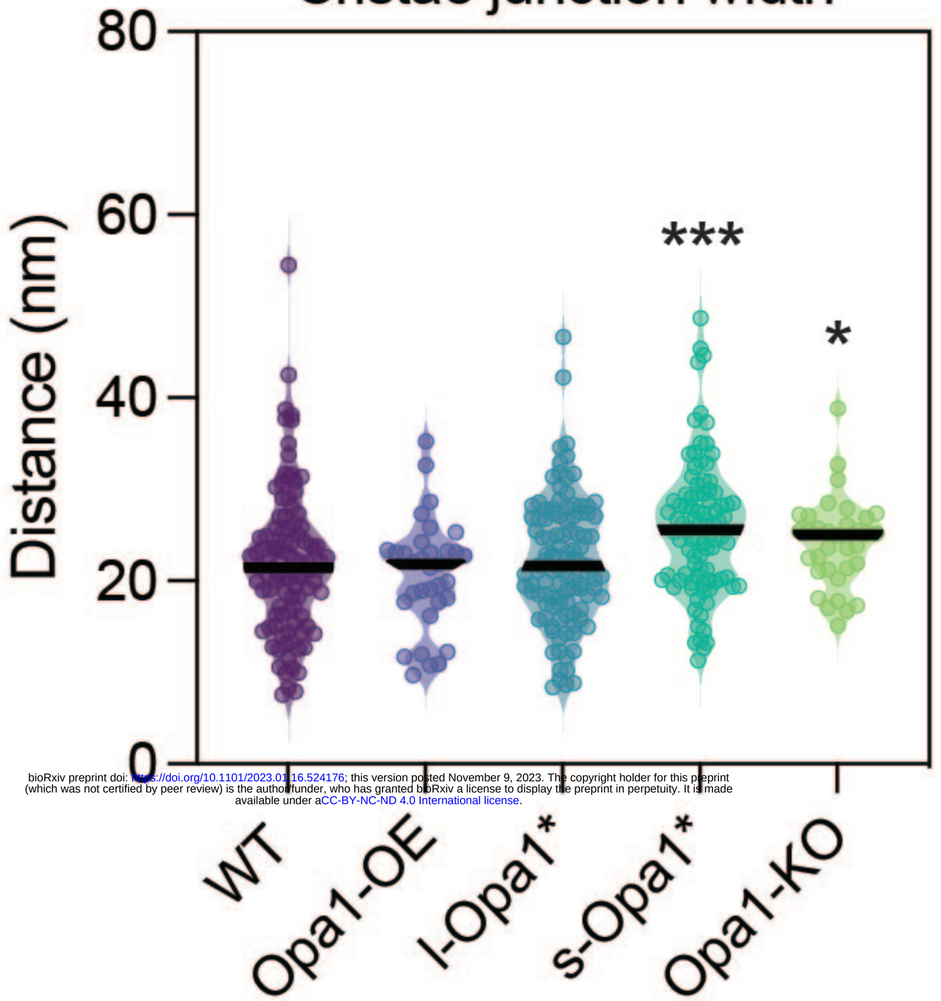

b

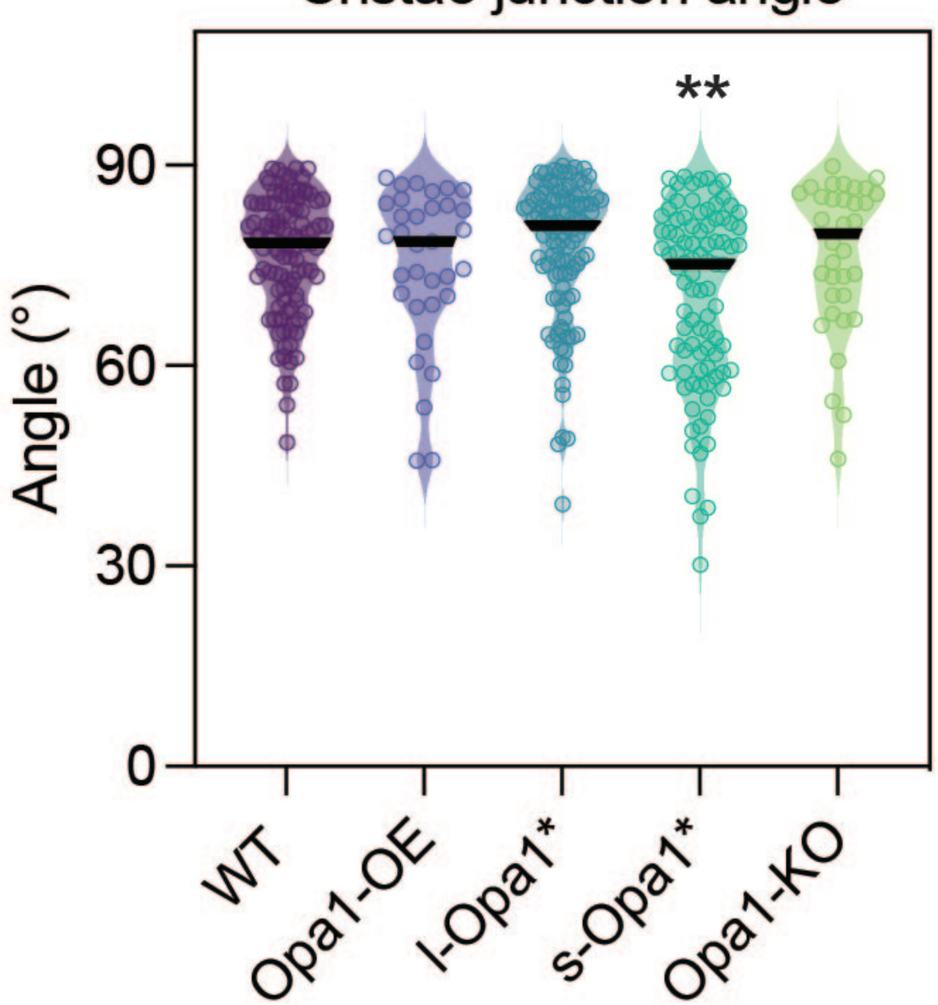

c

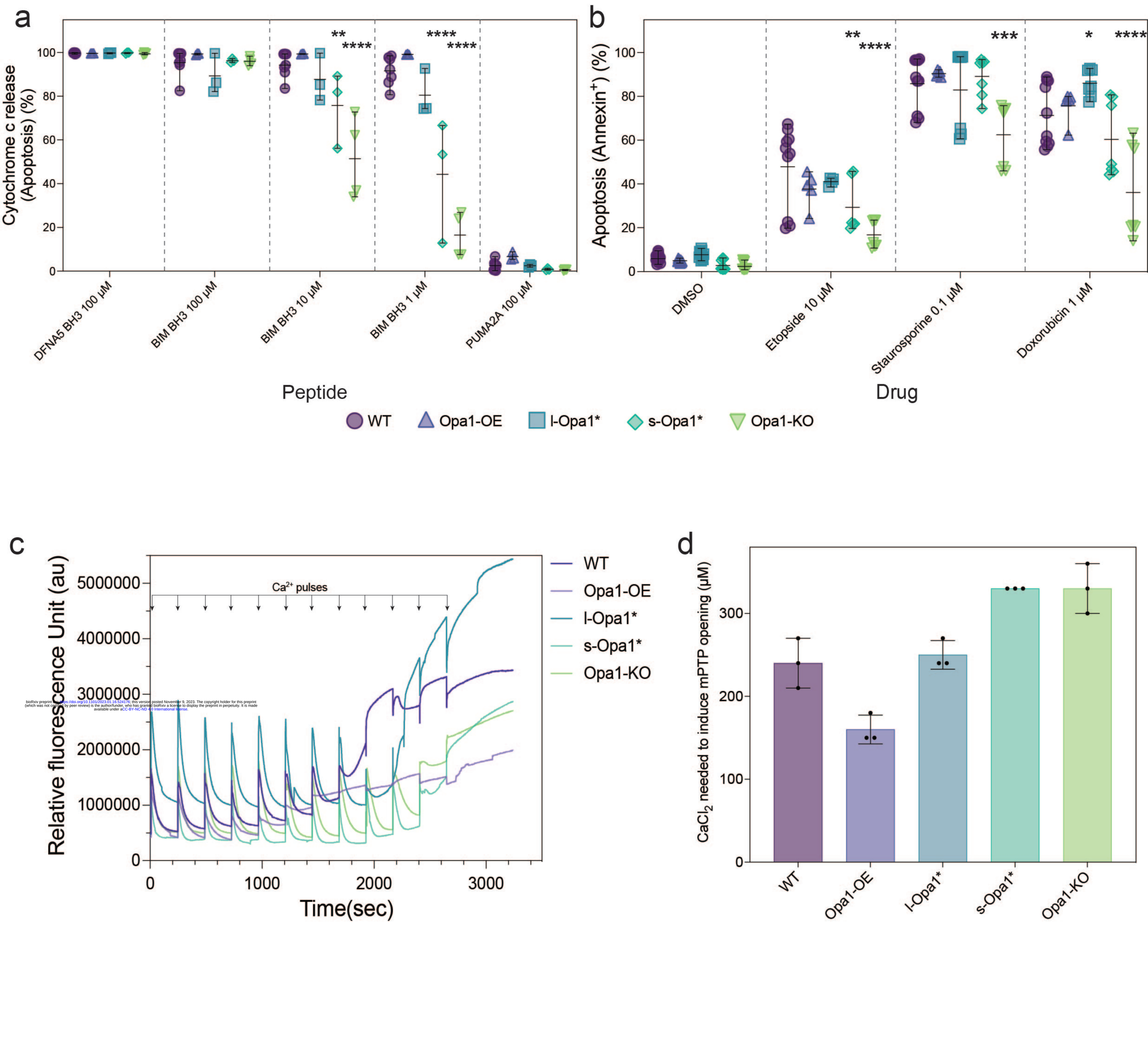

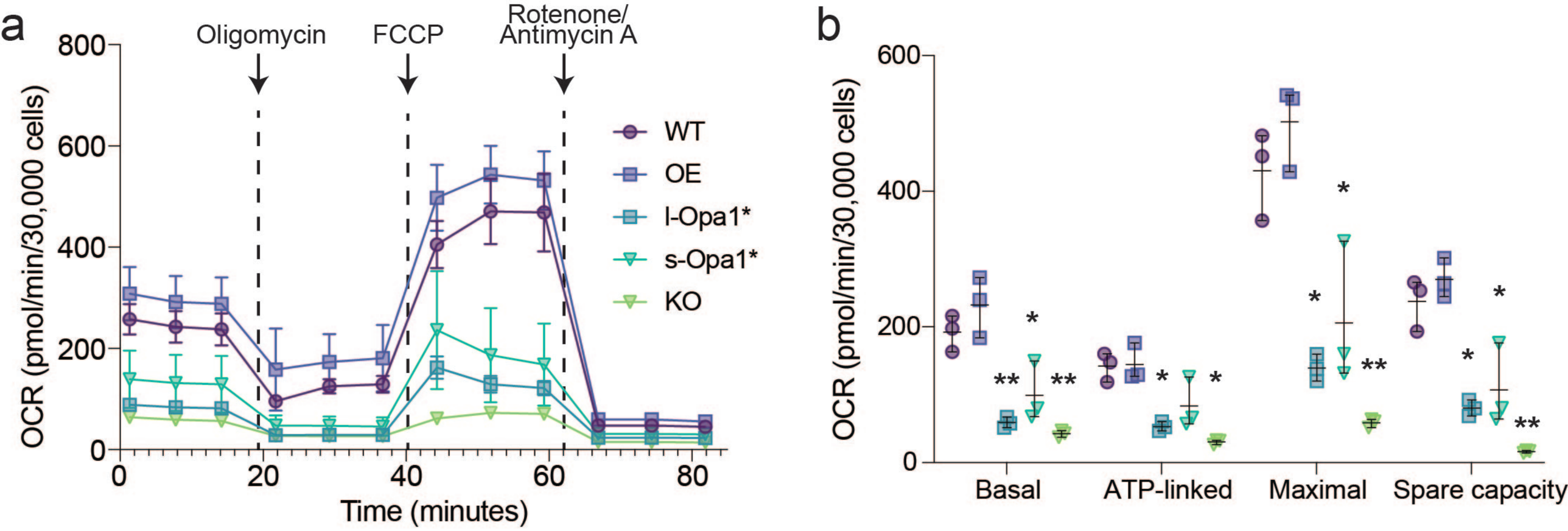
a
Oligomycin
FCCP
Rotenone/
Antimycin A
OCR (pmol/min/30,000 cells)
Time (minutes)
WT
OE
l-Opa1*
s-Opa1*
KO
b
OCR (pmol/min/30,000 cells)
Basal
ATP-linked
Maximal
Spare capacity

OMM

IMM

a. amorphous cristae may affect ETC assembly resulting in compromised respiration

l-Opa1*

Stacking cristae

multi-junction cristae

amorphous cristae

tubular cristae

s-Opa1*

WT CJ width and perpendicularity

b. abnormal apoptotic priming and calcium handling in mitochondria with wider CJs and vesicular cristae

c.

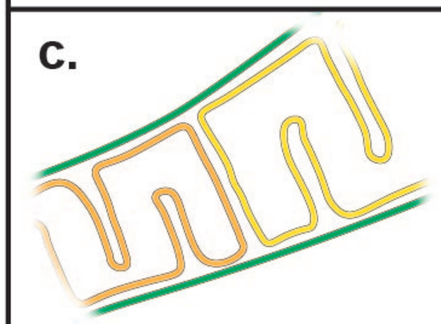

The presence of straight across multi-junction cristae in l-Opa1* may result from accumuluation of fusion intermediates

d.

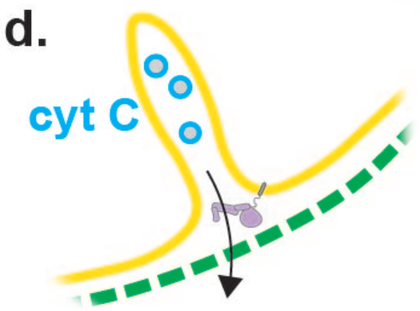

l-Opa1 at the cristae junction may perform a custodial role in mediating proper cytochrome C release transition & calcium handling

a

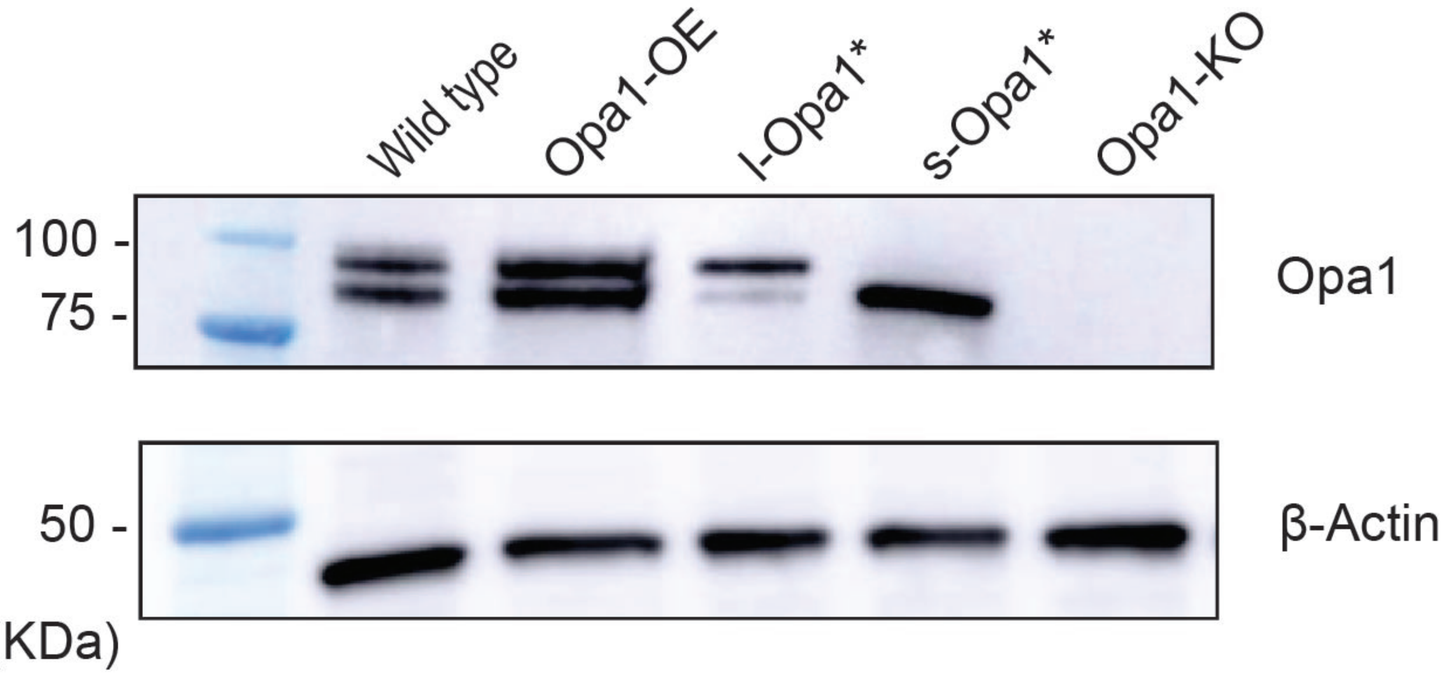

b

Name of line:	*Referred to in this study as:*	*Linear scheme for protein products produced:*	*Cartoon depiction of Opa1 form(s) present:*
WT MEF	WT	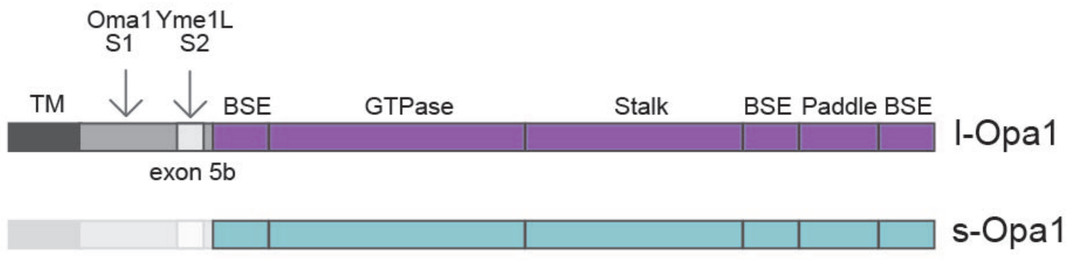	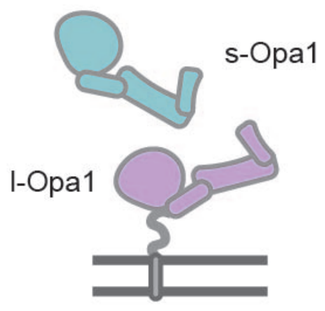
Stable Opa1-overexpressing MEF	Opa1-OE	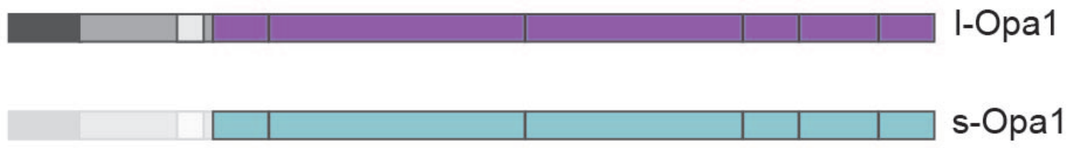	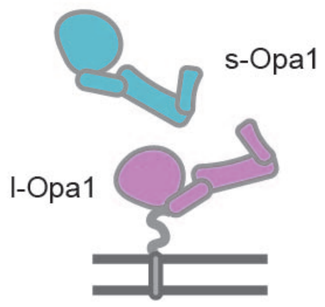
MEF CRISPR Δexon5b in Oma1$^{-/-}$ background	l-Opa1*	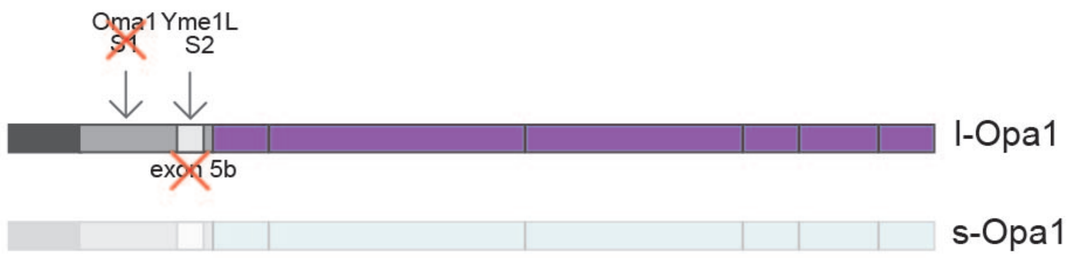	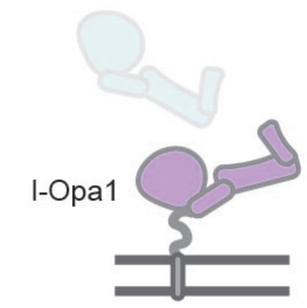
Opa1-KO MEF transfected with Opa1 isoform 5 only	s-Opa1*	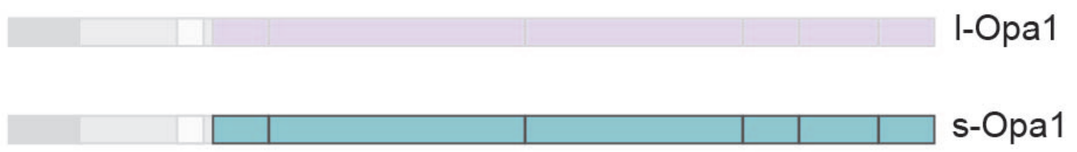	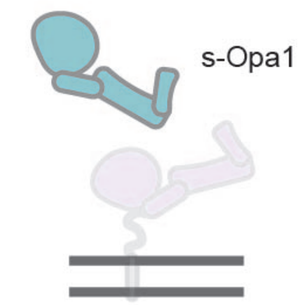
Opa1-KO MEF	Opa1-KO	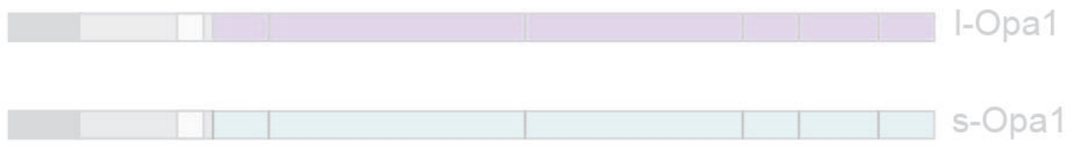	

a

WT

Opa1-OE

l-Opa1*

s-Opa1*

Opa1-KO

b

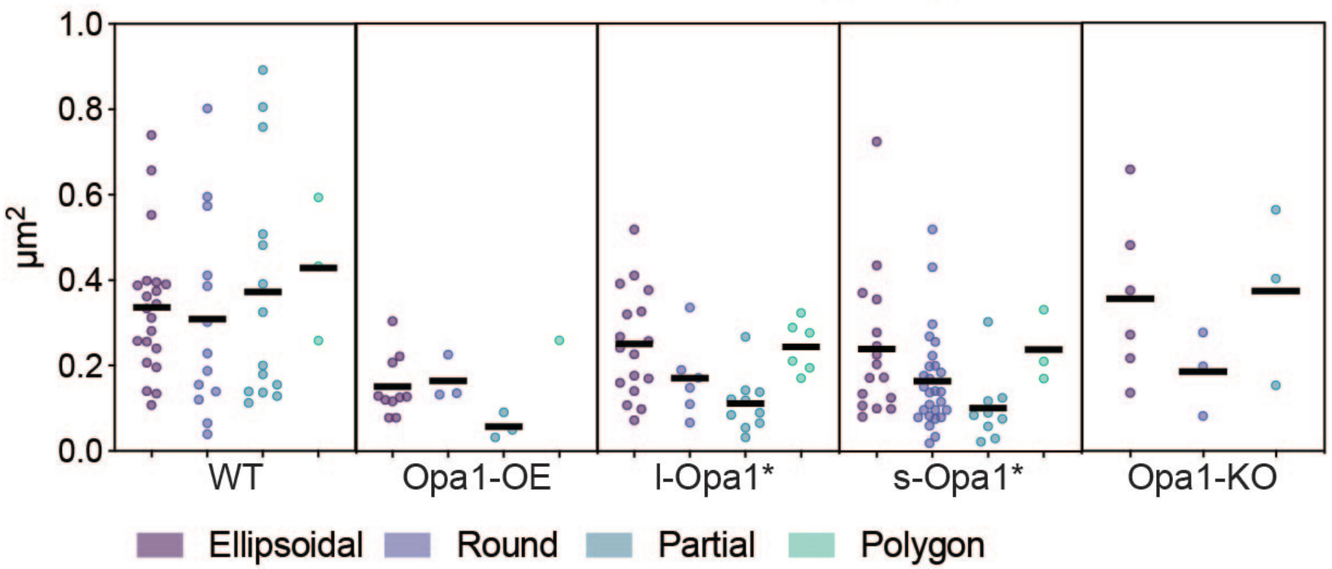

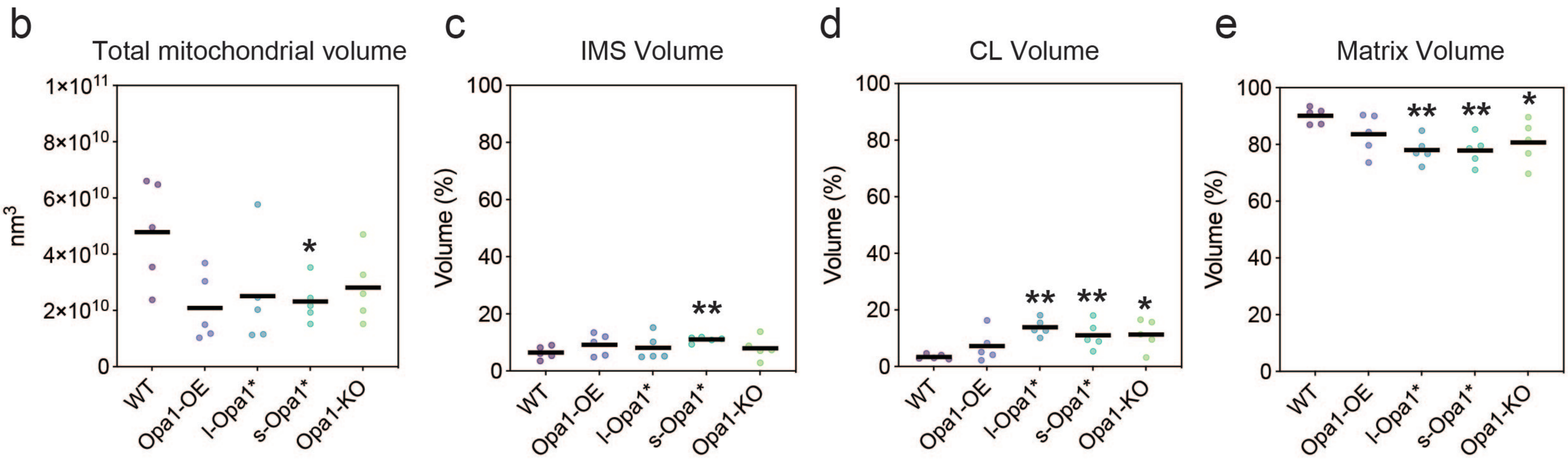

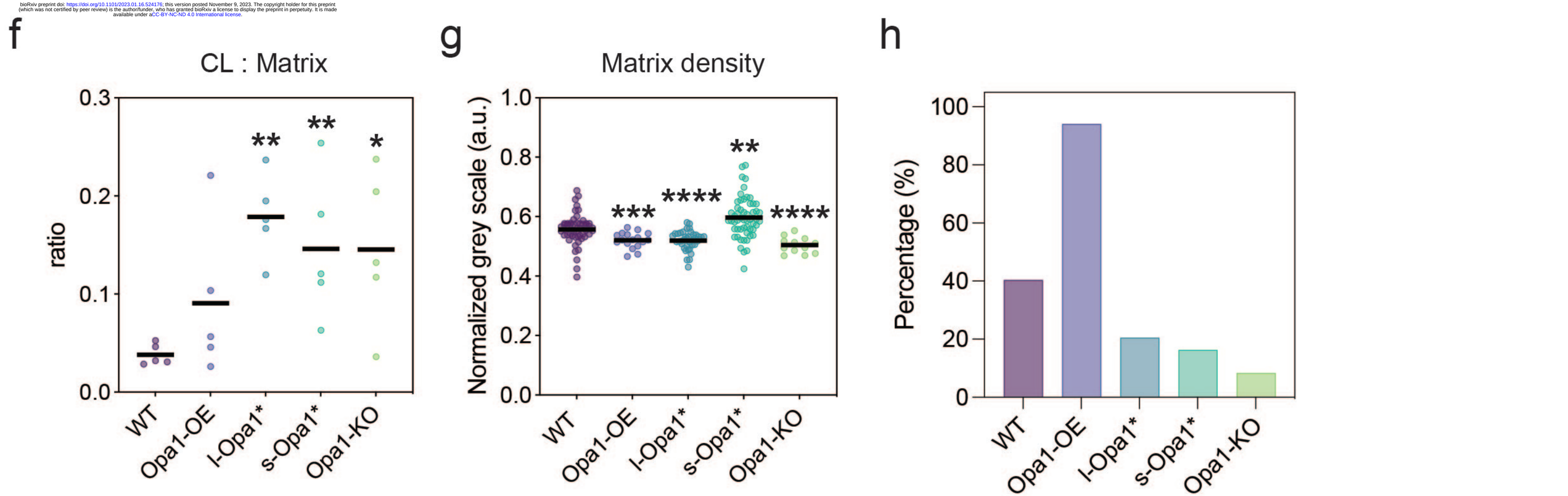

a

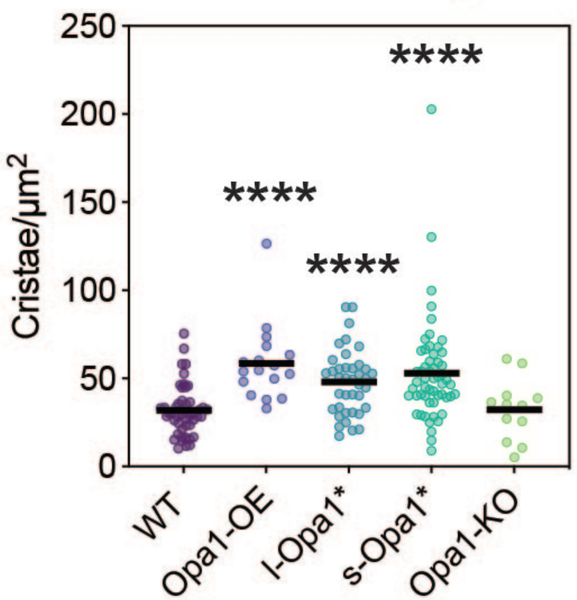

b

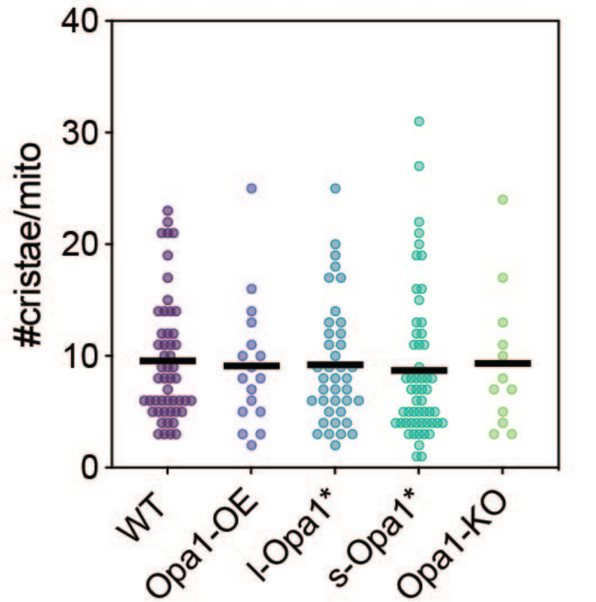

c

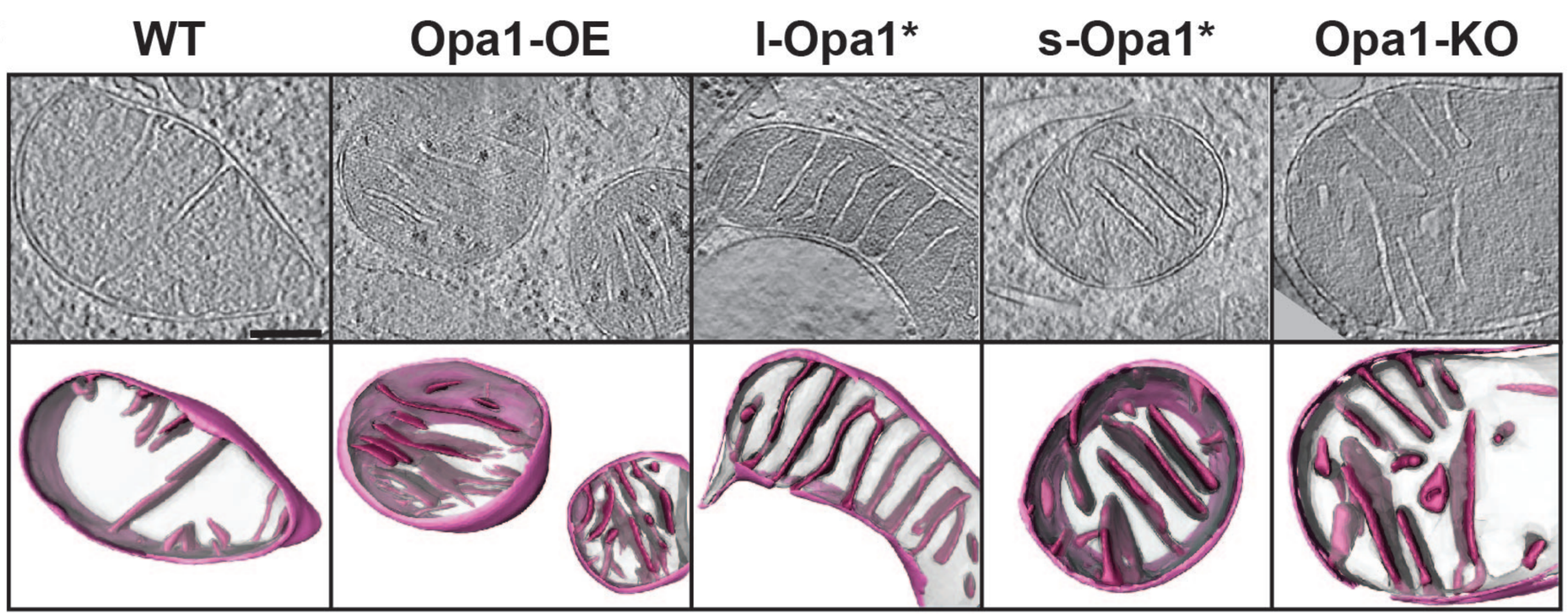

d

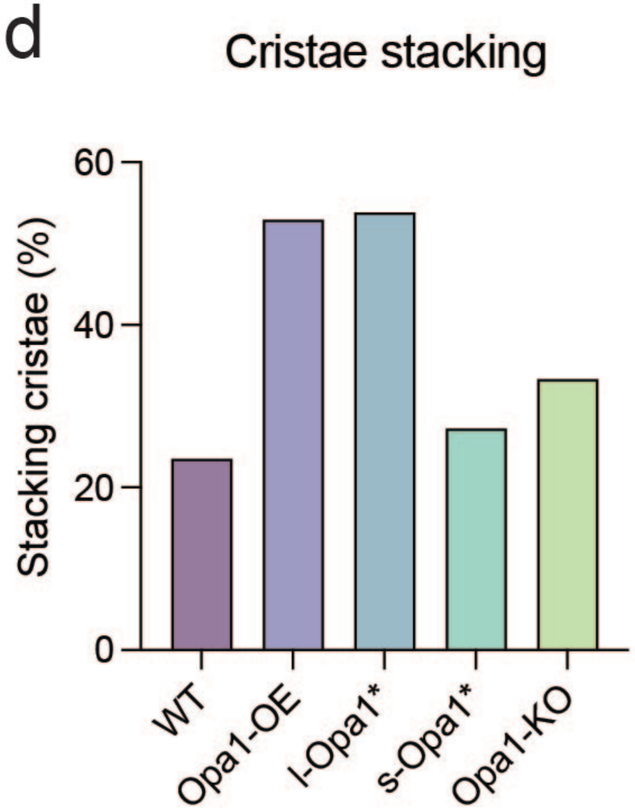

a

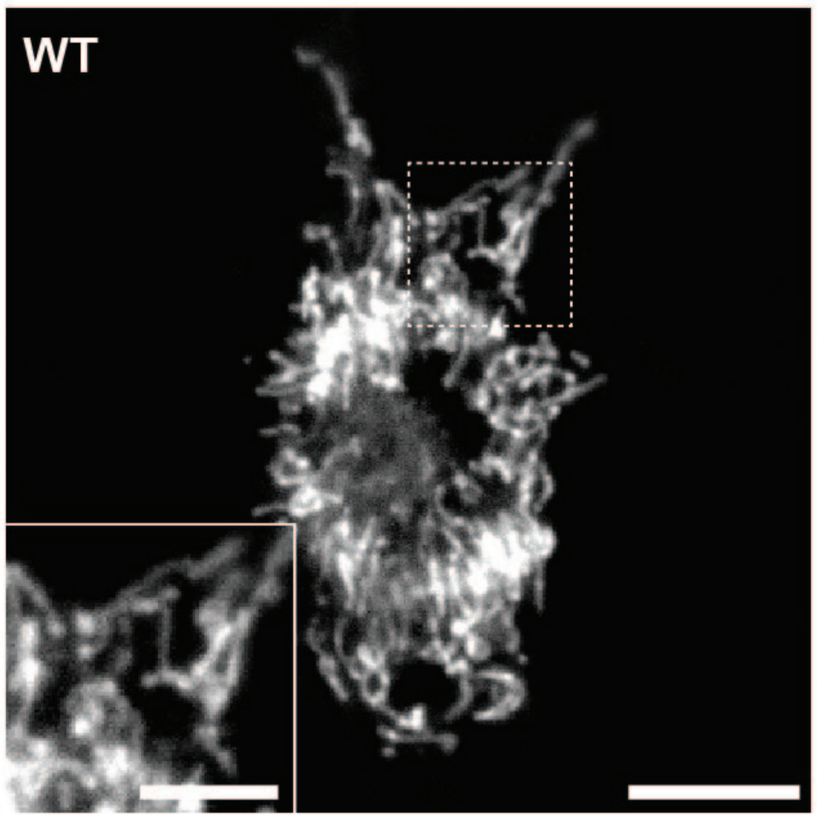

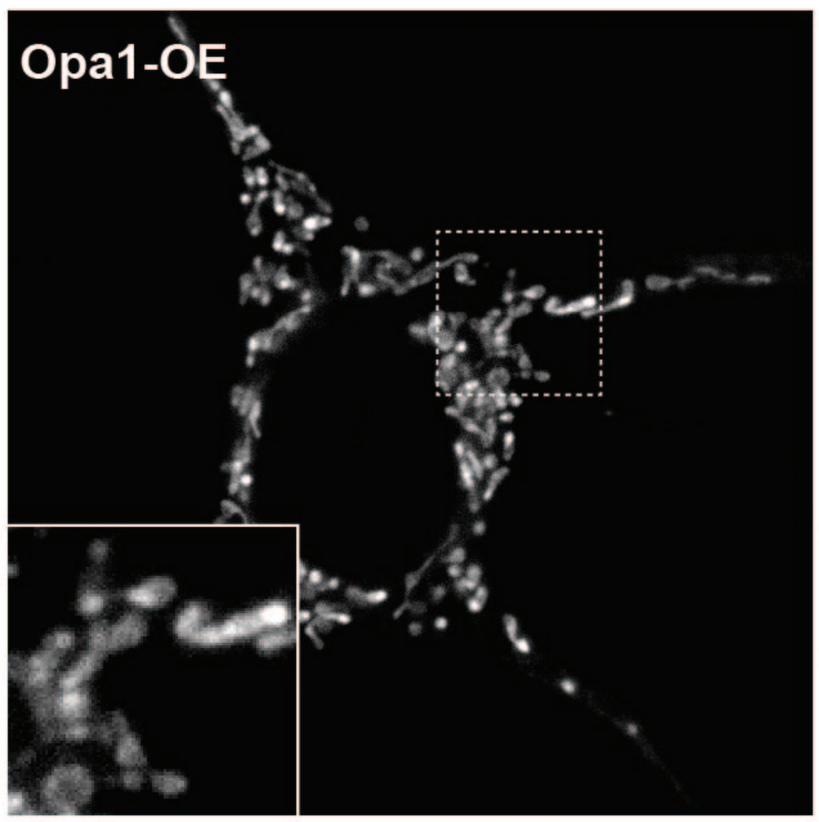

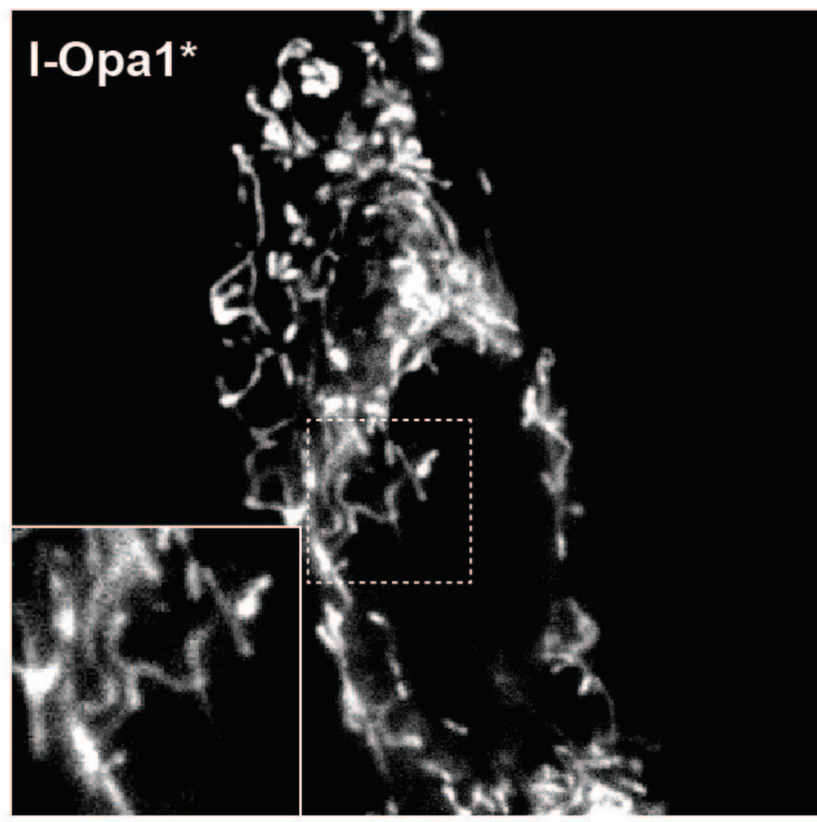

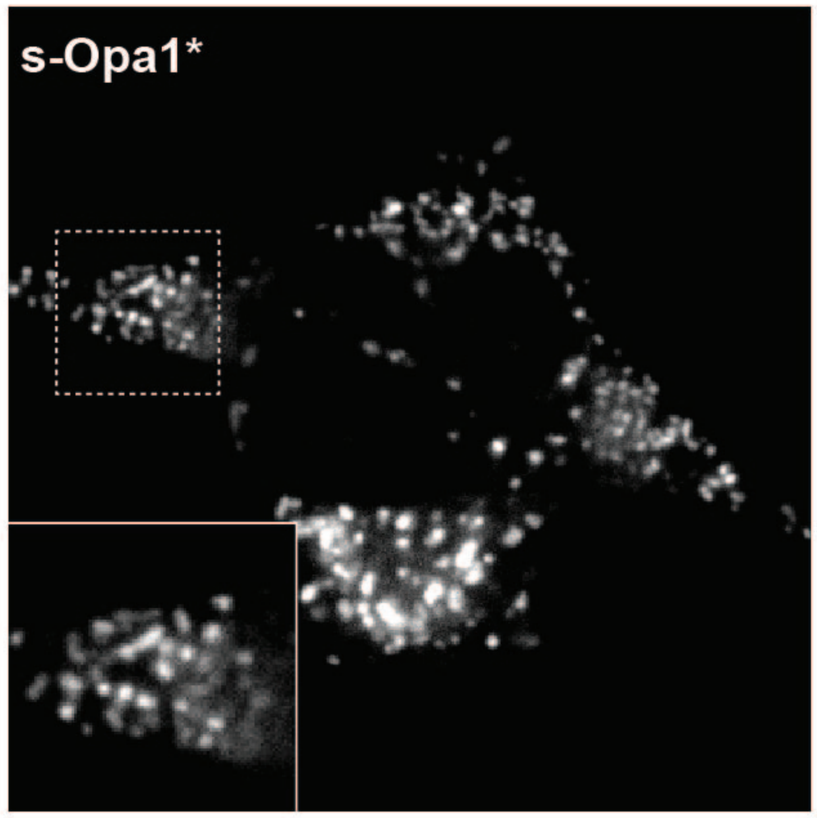

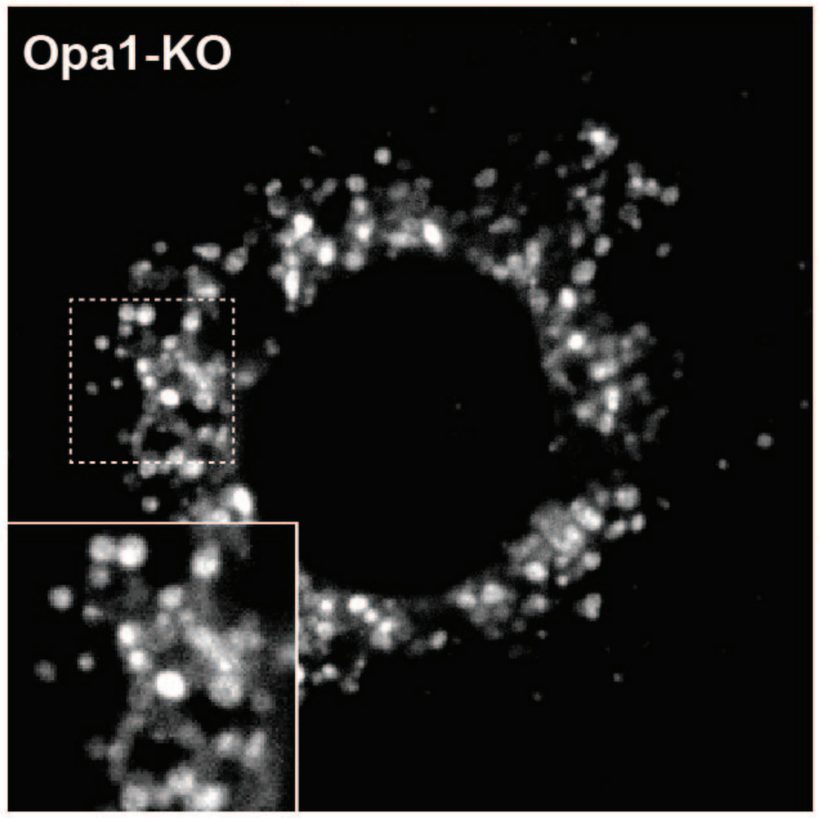

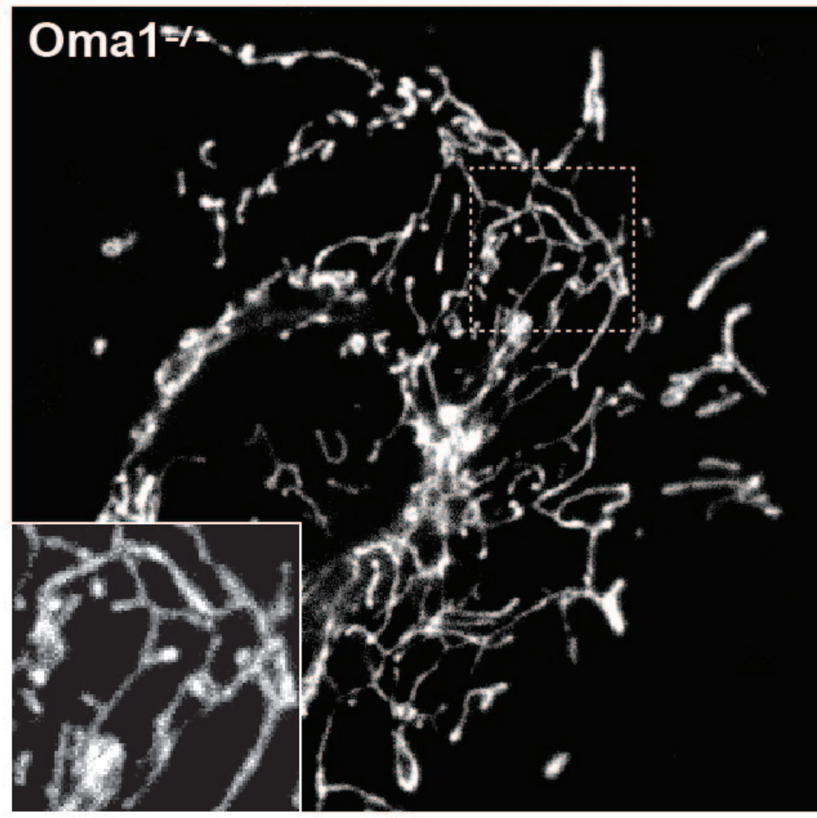

b

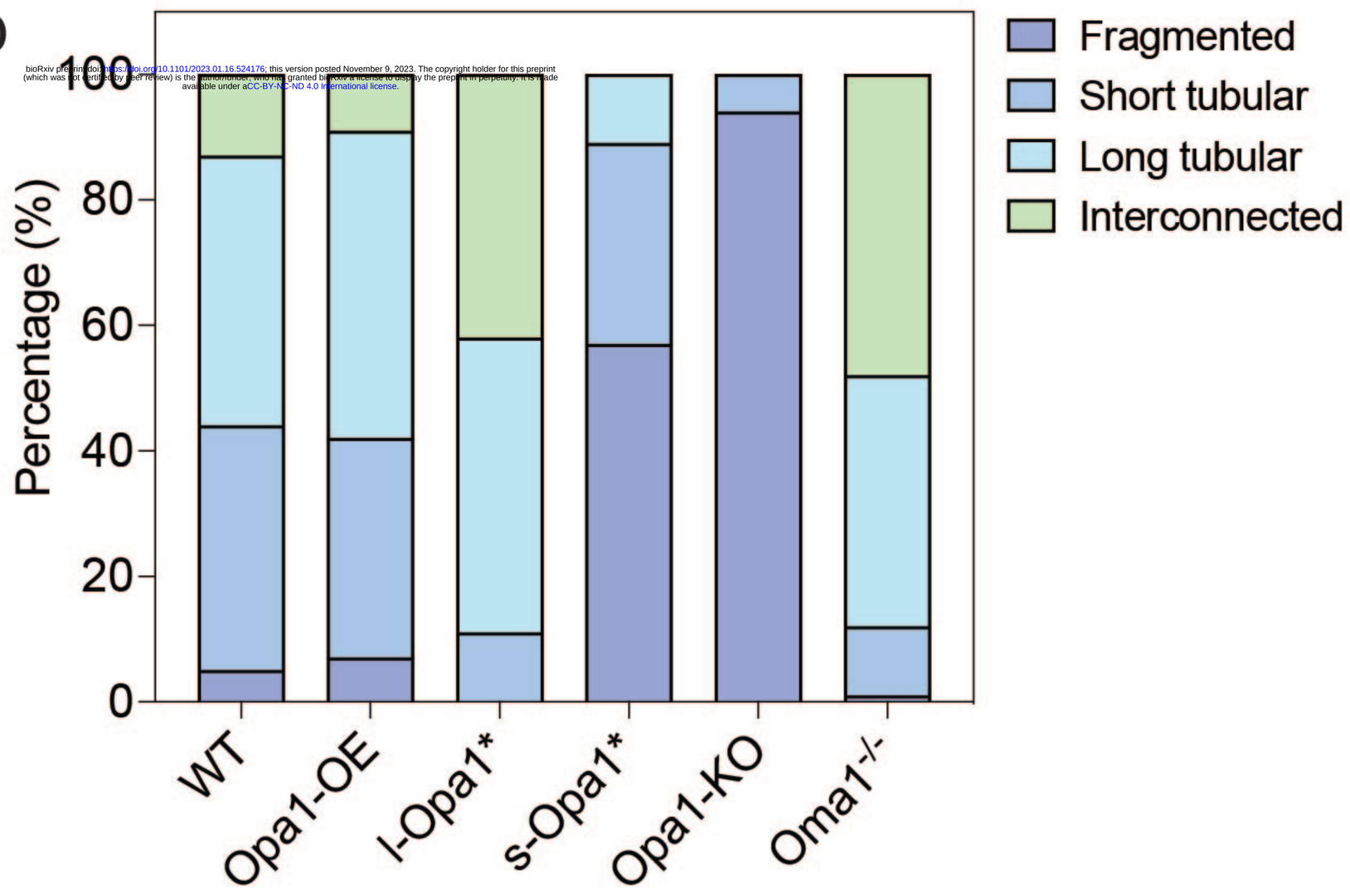

a

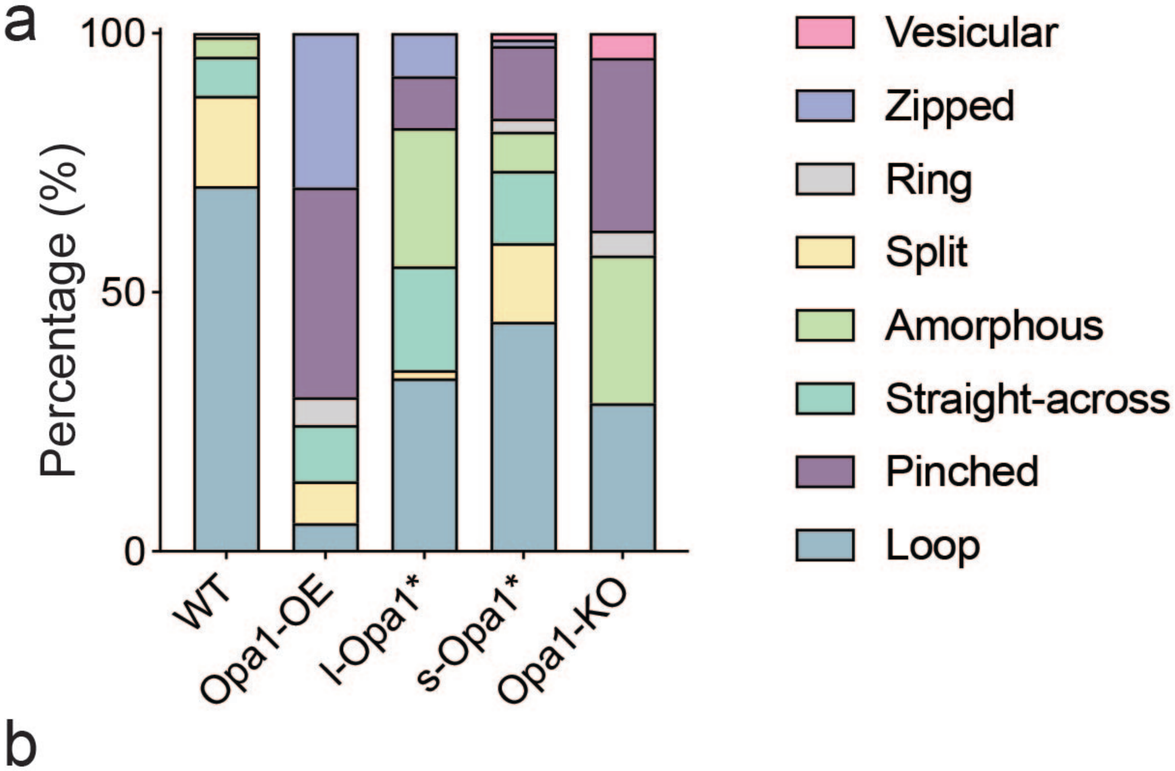

b

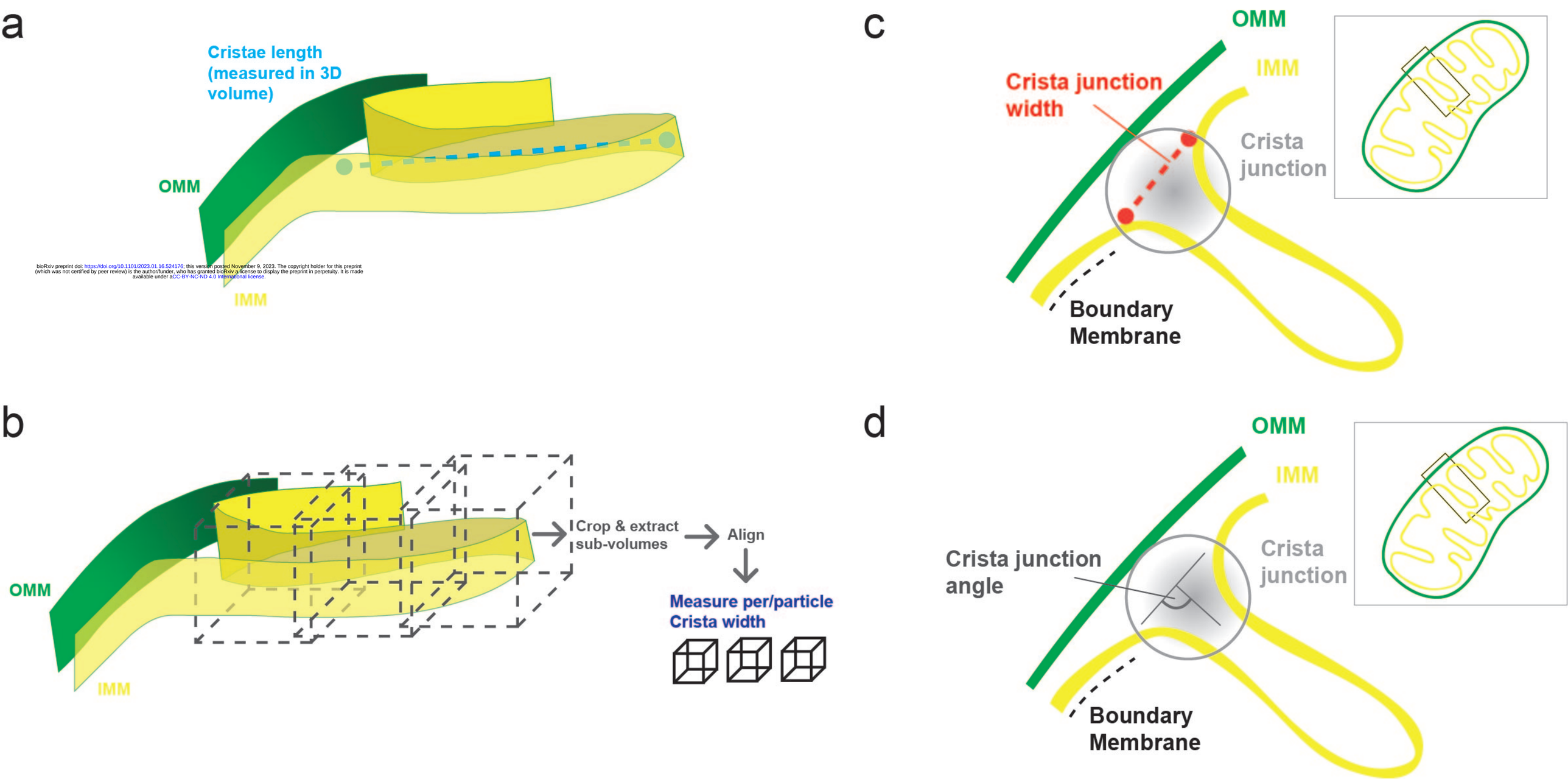

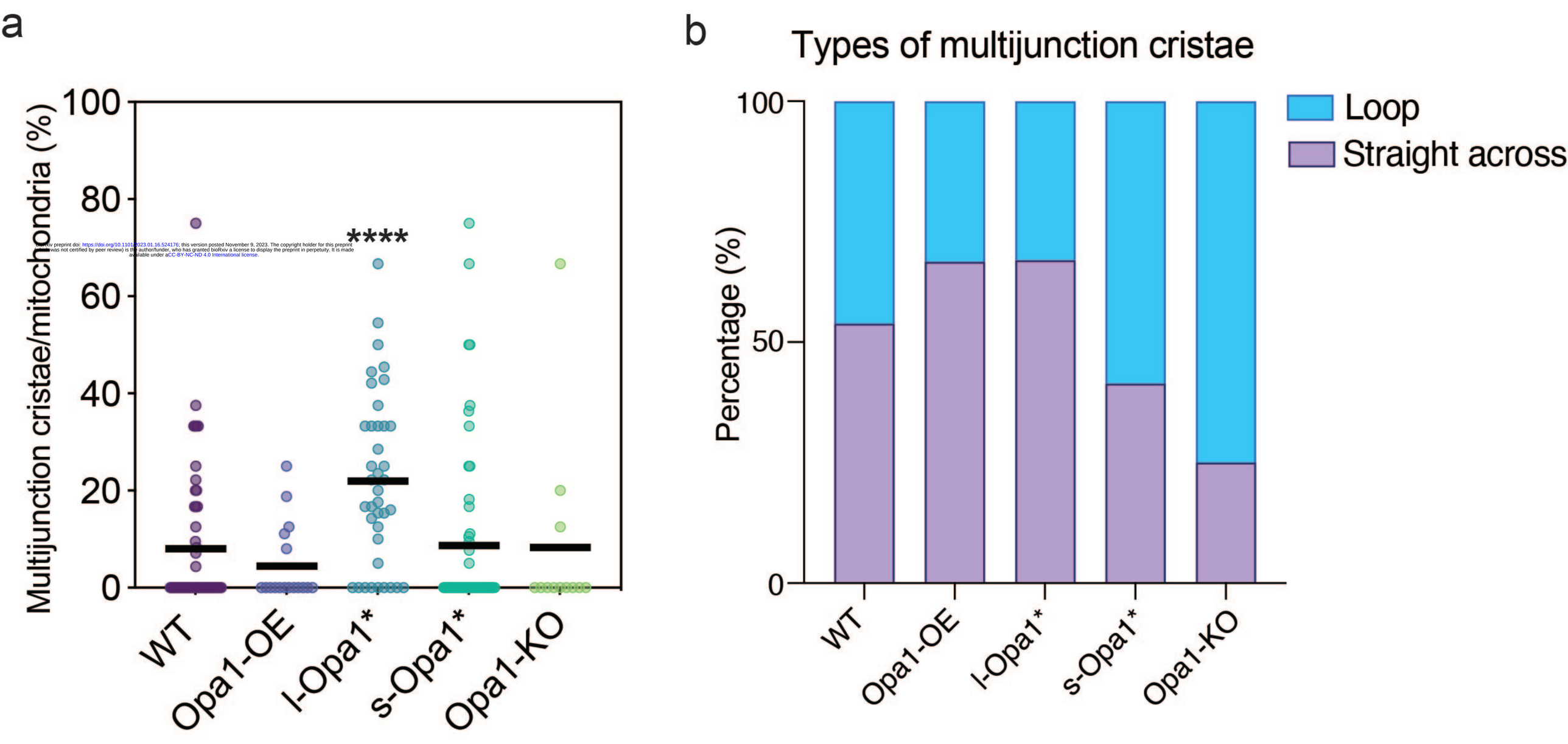

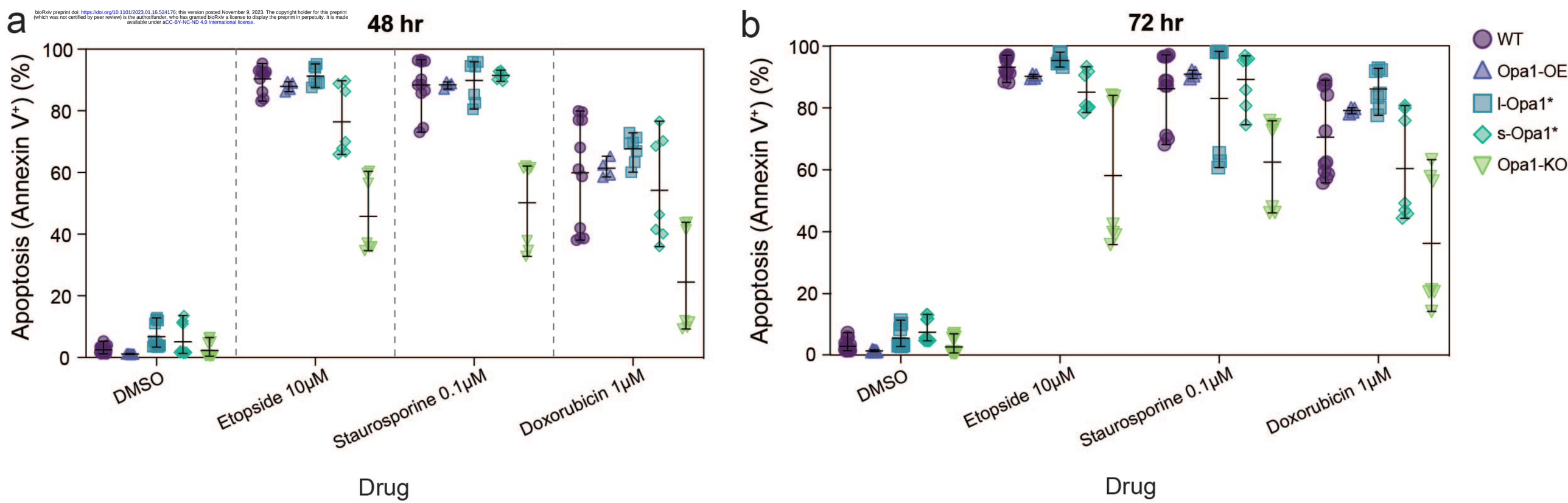

a

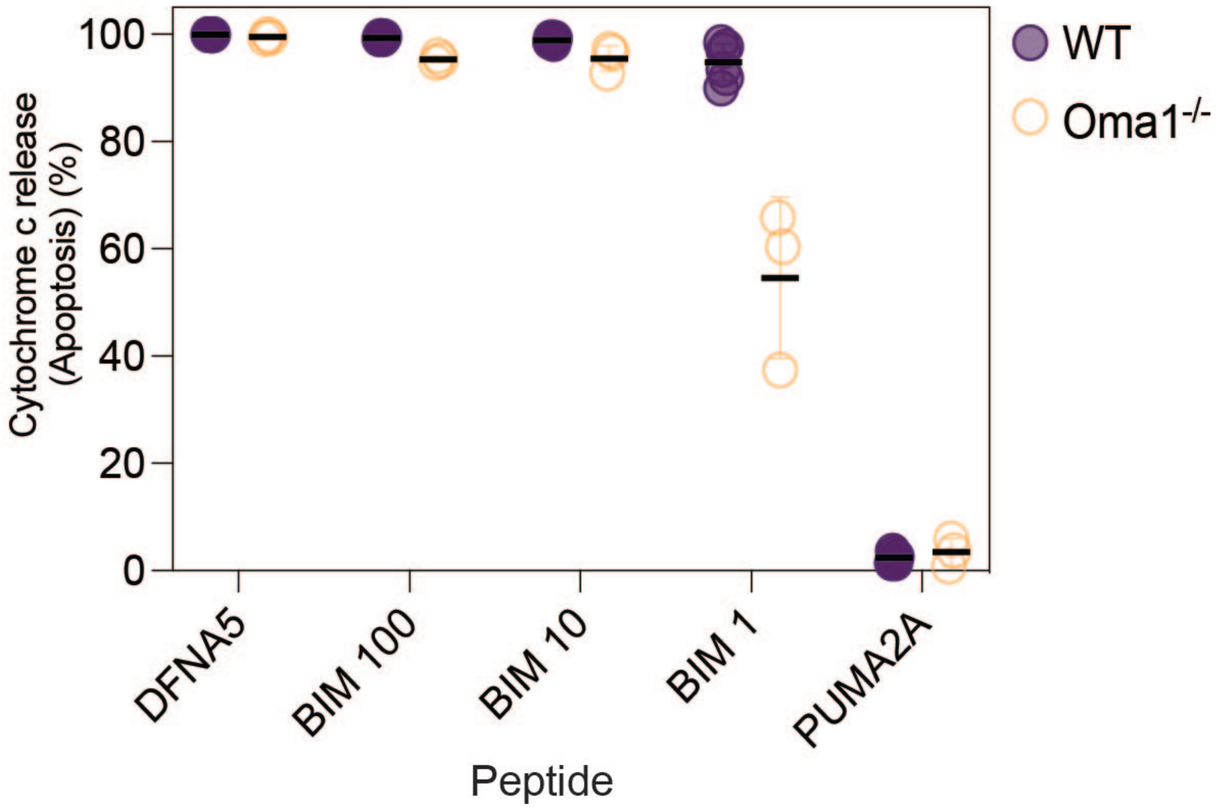

b

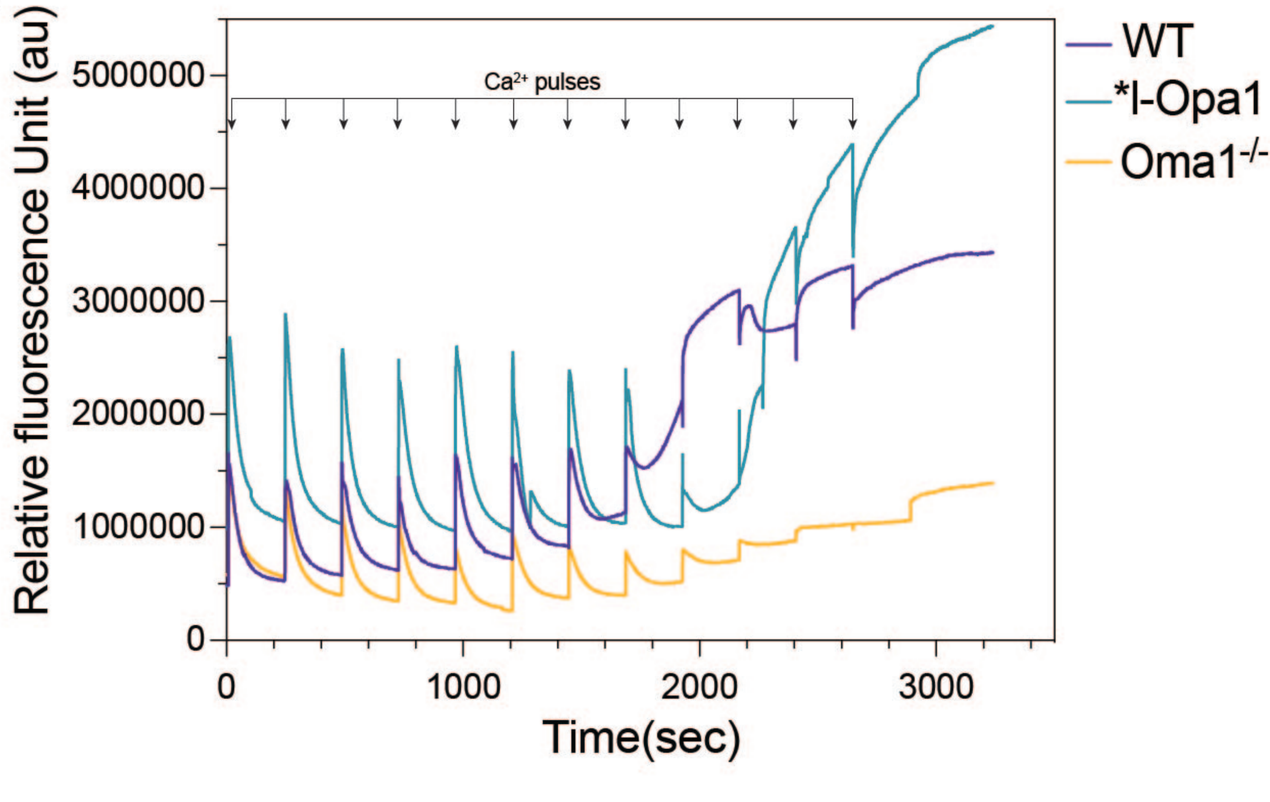

c

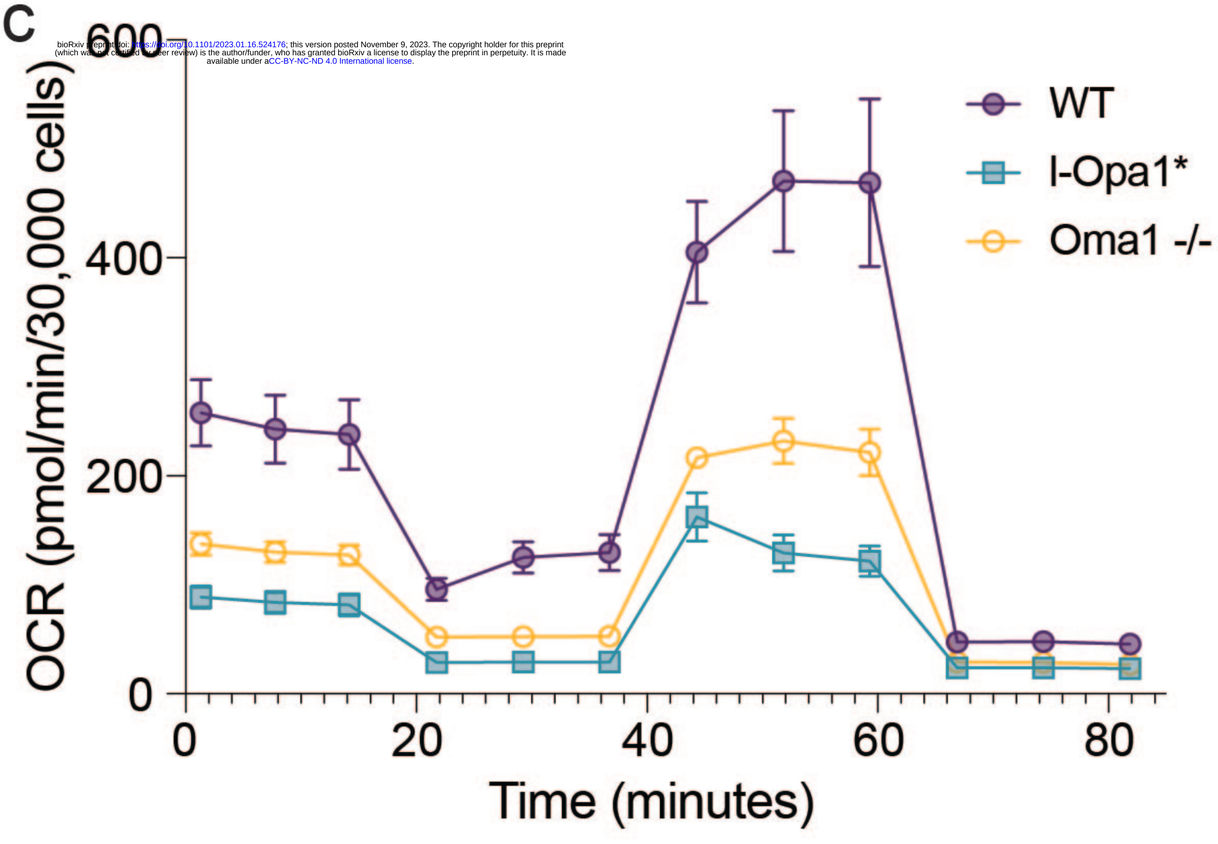

d

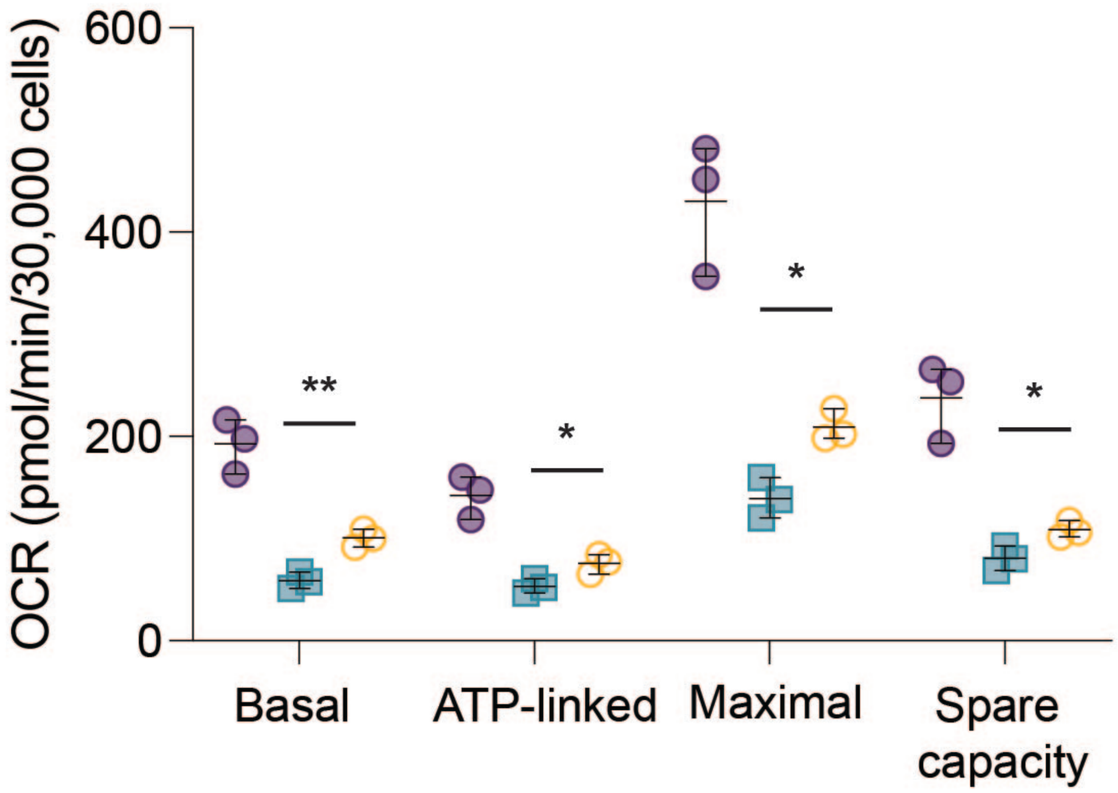

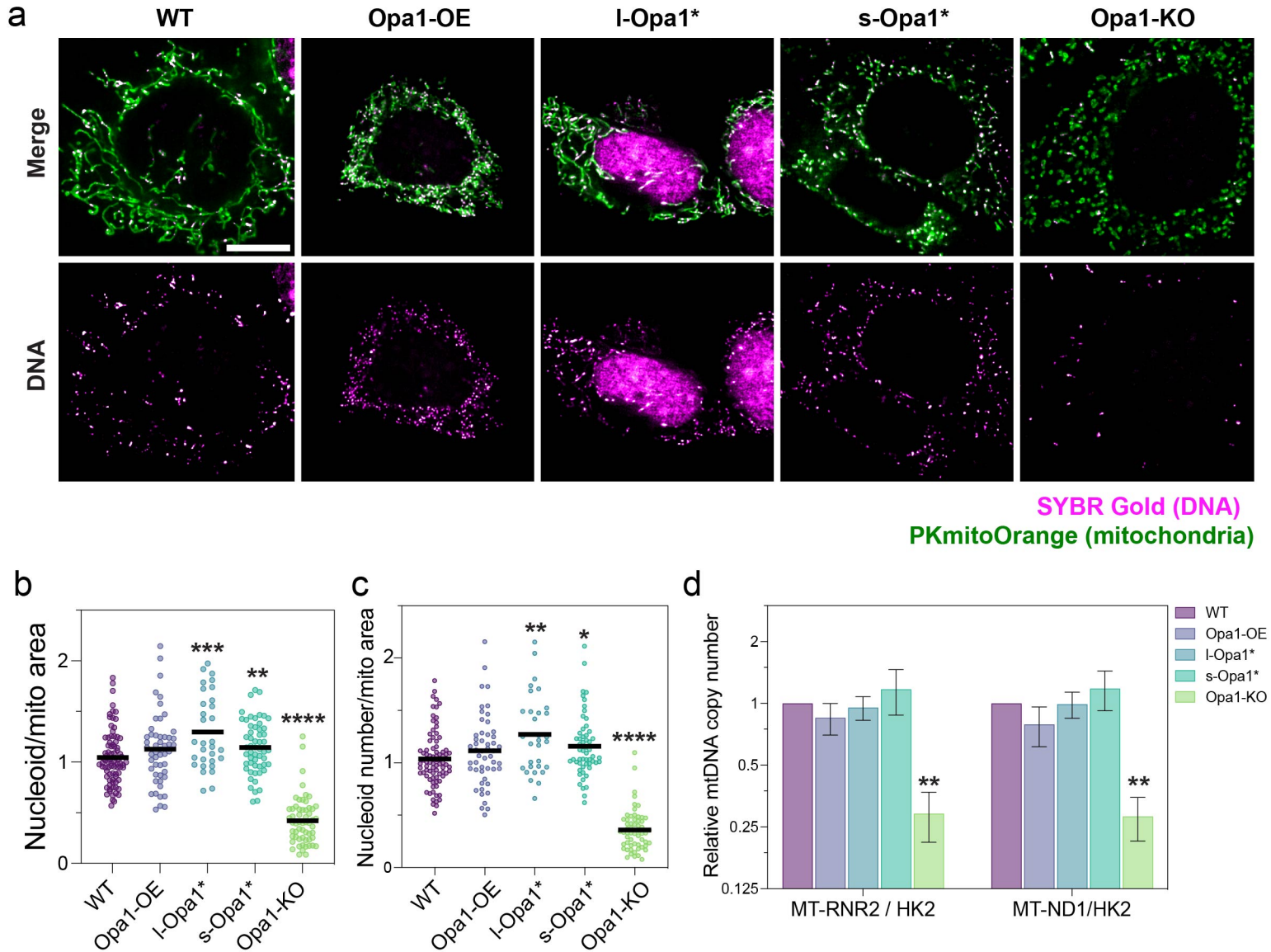
a
WT
Opa1-OE
l-Opa1*
s-Opa1*
Opa1-KO
Merge
DNA
SYBR Gold (DNA)
PKmitoOrange (mitochondria)
b
Nucleoid/mito area
0
1
2
***
**
****
WT
Opa1-OE
l-Opa1*
s-Opa1*
Opa1-KO
c
Nucleoid number/mito area
0
1
2
**
*
****
WT
Opa1-OE
l-Opa1*
s-Opa1*
Opa1-KO
d
Relative mtDNA copy number
0.125
0.25
0.5
1
2
**
**
MT-RNR2 / HK2
MT-ND1/HK2
WT
Opa1-OE
l-Opa1*
s-Opa1*
Opa1-KO

Supplementary Table 1. Summary of data acquisition and image processing for cryo-ET data in this study.

Sample		wt	Opa1-OE	l-Opa1*	s-Opa1*	Opa1-KO
Cryo-FIB milling	**Microscope**	Aquilos Cryo-FIB, FEI – Thermo Fisher Scientific	Aquilos Cryo-FIB, FEI – Thermo Fisher Scientific	Aquilos Cryo-FIB, FEI – Thermo Fisher Scientific	Aquilos Cryo-FIB, FEI – Thermo Fisher Scientific	Aquilos Cryo-FIB, FEI – Thermo Fisher Scientific
Acquisition settings	**Microscope**	Titan Krios Gi3 FEI, Thermo Fisher Scientific	Titan Krios Gi3 FEI, Thermo Fisher Scientific	Titan Krios Gi3 FEI, Thermo Fisher Scientific	Titan Krios Gi3 FEI, Thermo Fisher Scientific	Titan Krios Gi3 FEI, Thermo Fisher Scientific
	Voltage (KeV)	300	300	300	300	300
	Detector	Gatan K3 IS	Gatan K3 IS	Gatan K3 IS	Gatan K3 IS	Gatan K3 IS
	Energy filter	Gatan BioQuantum K3	Gatan BioQuantum K3	Gatan BioQuantum K3	Gatan BioQuantum K3	Gatan BioQuantum K3
	Slit width (eV)	20	20	20	20	20
	Super-resolution mode	Yes	Yes	Yes	Yes	Yes
	Å/pixel	2.076	2.076	2.076	2.076	2.076
	Defocus (µm)	-3.5 to -5.0	-3.5 to -5.0	-3.5 to -5.0	-3.5 to -5.0	-3.5 to -5.0
	Acquisition scheme	-70/70, 2°, Dose-symmetric	-70/70, 2°, Dose-symmetric	-70/70, 2°, Dose-symmetric	-70/70, 2°, Dose-symmetric	-70/70, 2°, Dose-symmetric
	Total dose	~90 - 120	~90 - 180	~90 - 180	~90 - 120	~90 - 120
	Dose rate (e-/Å/sec)	~ 2.5 – 3.5	~ 2.5 – 3.5	~ 2.5 – 3.5	~ 2.5 – 3.5	~ 2.5 – 3.5
	Frame number	6	6	6	6	6
	Number of tomograms	33	7	27	22	11
Image processing	**Frame alignment and dose weighting**	*framealign*, IMOD	*framealign*, IMOD	*framealign*, IMOD	*framealign*, IMOD[7]	*framealign*, IMOD[7]
	Tilt series alignment	IMOD	IMOD	IMOD	IMOD	IMOD
	WBP	IMOD	IMOD	IMOD	IMOD	IMOD
	Denoising	Topaz	Topaz	Topaz	Topaz	Topaz
	3D-segmentation	Amira	Amira	Amira	Amira	Amira
	3D-rendering	Amira	Amira	Amira	Amira	Amira